A study of crystal-site structure and solid-solution region of langasite-type oxide crystal with four elements

博士論文

A study of crystal-site structure and solid-solution region of langasite-type oxide crystal with four elements

(４元系ランガサイト型酸化物結晶の結晶サイト構造と固溶領域に関する研究)

Hengyu　Zhao

趙　衡煜

平成　　26 年

Contents

Chapter 1 Introduction

1.1 Langasite-type crystals

Crystalline langasite ($La_3Ga_5SiO_{14}$) is a well-known piezoelectric material and will be potentially used in pressure sensors [1,2] and surface acoustic wave (SAW) devices [3,4]. Langasite was initially studied as a candidate for laser devices [5-8].

Langasite-type oxide crystals have a structure of $A_3BC_3D_2O_{14}$ and belong to the trigonal system, point group 32, and space group *P*321; this crystal symmetry differs from that of quartz, $P3_121$ or $P3_221$ [9-11]. The schematic projections along [100], [010], and [001] orientations of the $A_3BC_3D_2O_{14}$-type structure are presented in Fig. 1.1. Here, A represents a dodecahedral site that is coordinated by 8 oxygen atoms, B is an octahedral site coordinated by 6 oxygen atoms, and both C and D represent tetrahedral sites coordinated by 4 oxygen atoms, where the D site is slightly smaller than the C site.

Langasite as a piezoelectric crystal is superior to quartz and $LiTaO_3$. High stability of SAW velocity for temperature change and large electro-mechanical coupling factor are required the substrate of SAW devices. Quartz shows high temperature stability but small electro-mechanical coupling factor, while $LiTaO_3$ shows large coupling factor but small temperature stability. Langasite crystals show relatively high temperature stability and large coupling factor. The electro-mechanical coupling factor of langasite is approximately three times that of quartz, and langasite also has a wider working temperature range [12], which indicates good piezoelectric properties for SAW devices. Another advantages of LGS is lack of a Curie point, that is, no change of crystal structure until its melting point at 1470 ℃.

Langasite-type crystals with $A_3BC_3D_2O_{14}$ structure that can be differentiated into ordered and disordered types. In the ordered structure, each site is occupied by only one element, as is the case in $Ca_3TaGa_3Si_2O_{14}$ (CTGS), $Sr_3NbGa_3Si_2O_{14}$ (SNGS), $Ba_3TaAl_3Si_2O_{14}$ (BTAS) and other materials [13] in which four elements are found at each of the A, B, C and D cation sites. However, not all the langasite-type crystals occur in ordered structures. In the disordered structures, cation sites may be occupied by two or more elements. In langasite, for example, La occupies the A site, while Ga occupies the B and C sites and half of the D site, with Si sharing the other half of the

D site. The unfixed occupancy of the D site produces a disordered structure in langasite crystals. All langasite-type crystals with three elements exhibit disordered structures, including langasite, langatate ($La_3Ta_{0.5}Ga_{5.5}O_{14}$) and langanite ($La_3Nb_{0.5}Ga_{5.5}O_{14}$). To evaluate and optimize the future high temperature applications of these langasite-type materials, significant effort has been applied to studying their piezoelectric behavior, sensitivity and electric conductivity between ambient and high temperatures up to 600 ℃. These studies have indicated that langasite-type crystals with ordered structures show better performance than either disordered langasite or semi-ordered langatate at elevated temperatures [14].

$Ca_3TaGa_3Si_2O_{14}$ (CTGS) is one of the most promising candidates for applications in high temperature pressure sensors, since it consists of four elements and thus is expected to present an ordered crystal structure.

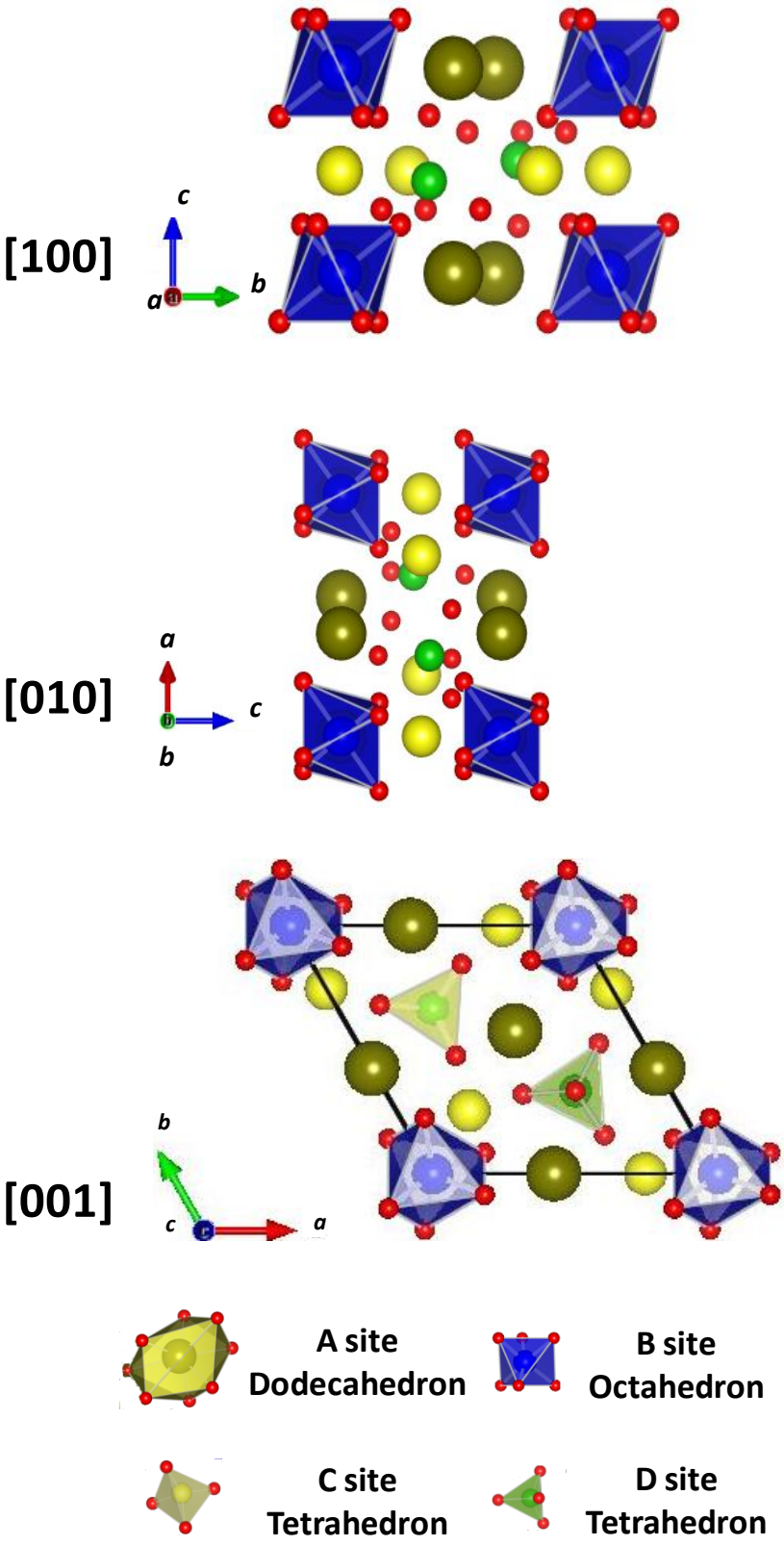

Fig. 1.1 Projection of the $A_3BC_3D_2O_{14}$ structure along [100], [010], and [001].

1.2 $Ca_3TaGa_3Si_2O_{14}$ (CTGS) used as a high-temperature pressure sensor

To reduce both fuel consumption and CO_2 emissions, the automotive industry requires highly efficient pressure sensors capable of precisely monitoring combustion parameters in vehicle engines [15]. The piezoelectric crystals employed in such pressure sensors must have a high electrical resistivity at elevated temperatures [16] since high temperatures typically result in drastic decreases in the electrical resistivity of the bulk crystal [17], which can potentially degrade the electric circuitry of the pressure sensor. Specifically, the bulk crystal electrical resistivity required for applications in an engine combustion chamber is at least 10^{10} Ω•cm at temperatures up to 400 ℃ [18].

The application of high-temperature piezoelectric crystals faces a challenge with respect to the working temperature window of the candidate material. Materials' inherent phase instability, which causes an irreversible degradation of the device at high temperatures, must be considered. Great effort has been devoted to the selection of an appropriate piezoelectric crystal. However, suitable candidate crystals that exhibit no phase transition until their melting point and have a wide working temperature window are rare [19,20]. In the case of ferroelectric materials, the crystals will revert to their paraelectric phase and exhibit no piezoelectric properties when the temperature exceeds their Curie point (T_C). Perovskite-type crystals, which have an ABO_3 structure including $LiNbO_3$, $LiTaO_3$, and $Pb(Zr,Ti)O_3$, exhibit a phase transition from ferroelectric to piezoelectric properties. Non-ferroelectric piezoelectric crystals may also exhibit phase-transition problems. For instance, when quartz undergoes a phase transition at 573 ℃, the piezoelectric constant d_{11} vanishes and constant d_{14} remains; this leads to discontinuity in the piezoelectric behavior of the bulk crystal and limits the working temperature window [14].

For several reasons, high electrical resistance is required for high-temperature pressure sensors. The circuit of a pressure sensor equipped with an amplifier and a piezoelectric crystal is shown in Fig. 1.2. First, when the resistance of the piezoelectric crystal (R') is lower than that of the amplifier (R), the circuit is disabled because piezoelectric charges are drained before being detected by the circuit [14]. The duration time of the piezoelectric charge is proportional to product of RC, where

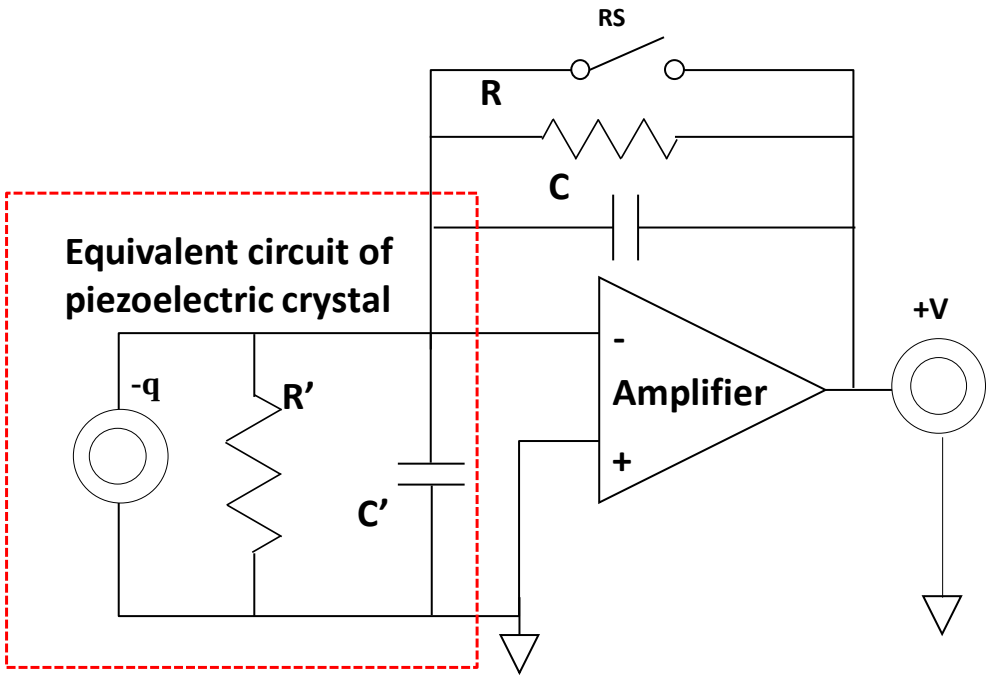

Equivalent electric circuit of pressure sensor

Fig. 1.2 Schematic of the circuit of a high-temperature pressure sensor. R' should be sufficiently larger than R.

C represents the capacitance of the piezoelectric crystal. Second, the minimum working frequency of a pressure sensor, which is known as the lower limiting frequency (f_{LL}), is inversely proportional to the *RC* time constant (Eq. 1.1). With a high electrical resistance, the dynamic bandwidth of the sensor is extended to frequencies as high as sonic frequencies [21-24]. In addition to the requirement of a stable circuit, a high electrical resistivity in the bulk crystal is required to suppress the electrical loss and noise level of the sensor.

$$f_{LL} = (2\pi RC)^{-1} \tag{1.1}$$

$$\rho = \rho_0 \exp\left(-\frac{E_a}{kT}\right) \tag{1.2}$$

The electrical resistivity ρ of piezoelectric crystals exhibits a temperature dependence (1000/*T*) that can be expressed by the Arrhenius law (Eq. 1.2), where *k* is the Boltzmann constant and E_a is the activation energy. Considering the importance of high resistivity and the practical requirements of industry, the desired electrical resistivity (ρ value) of a piezoelectric crystal used for high-temperature sensors should be greater than 10^{10} Ω•cm at temperatures up to 400 ℃ [18].

Notably, in addition to the important issues of high electrical resistivity at elevated temperatures, the temperature dependence of resistivity, and the phase stability of the bulk crystal, other issues that confront piezoelectric crystals at elevated temperatures include the thermal instability of the piezoelectric, dielectric, and electromechanical properties and chemical instability (i.e., decomposition). These factors need to be considered when optimizing high-temperature piezoelectric crystals; however, the factors will not be discussed in this study.

In addition to the survey on the characterization of piezoelectric behavior, sensitivity, and electric conductivity in langasite-type crystals [14], Yaokawa et al. have investigated the mechanism of the electrical conductivity of langasite-type crystals. The electrical conduction mechanism of LTG from room temperature to 600 ℃ involves the ionization of neutral Ta vacancies in the B site ($V_{\mathrm{Ta}}^{\times}$). A neutral Ta vacancy ($V_{\mathrm{Ta}}^{\times}$) formed by the incorporation of oxygen at the oxygen lattice position (illustrated in Eq. 1.3 and Fig. 1.3) will be ionized to yield holes (Eq. 1.4) [25]:

$$\frac{5}{4}\mathrm{O}_2 \leftrightarrow V_{\mathrm{Ta}}^{\times} + \frac{5}{2}\mathrm{O}_{\mathrm{O}}^{\times}, \tag{1.3}$$

$$V_{\mathrm{Ta}}^{\times} \leftrightarrow V_{\mathrm{Ta}}^{\mathrm{n}} + \mathrm{n}h^{\cdot}, \tag{1.4}$$

where n represents the maximum number of holes that one metal vacancy can release and is equal to the valence of the cation. They further revealed that the concentration of holes increases with the increasing degree of the ionization of $V_{\mathrm{Ta}}^{\times}$ due to the temperature increase while the concentration of $V_{\mathrm{Ta}}^{\times}$ was constant under certain oxygen atmosphere. Thus, from the previous study on the conduction mechanism of LTG, we understand that the location of metal vacancies can dramatically affect the electrical conductivity at elevated temperatures [25].

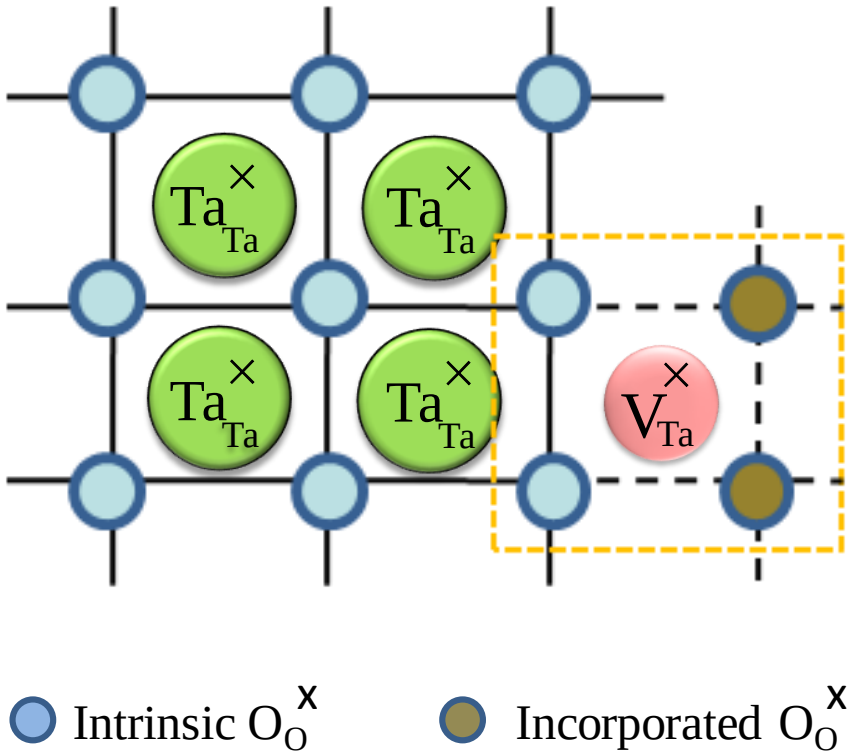

Fig. 1.3 Schematic of the formation of $V_{\mathrm{Ta}}^{\times}$ due to the incorporation of oxygen.

1.3 Growth of CTGS crystals

In the aspect of crystal growth, although several groups have grown good quality CTGS crystals via the Czochralski technique without reporting the occurrence of secondary phases [26-29], this does not mean an absence of secondary phases since they could hide somewhere in the melt apart from the growing crystal. In contrast, in the micro-pulling-down (μ-PD) method, all of the melt is consumed so that there is nowhere for secondary phases to hide. Yokota et al. [30] reported the occurrence of a Ca-Ta oxide material appearing in the peripheral portion of a CTGS crystal growing from a stoichiometric melt. There may be several possible reasons for the occurrence of secondary phases. One possibility is if the stoichiometric composition is close to the solid-solution boundary as is the case with $LiNbO_3$ [31], in which the stoichiometric melt changes its composition during growth and happens to reach the eutectic point, yielding a secondary phase other than $LiNbO_3$. In the case of CTGS, even the stoichiometric composition may not belong in the solid-solution region. Thus, it is important to determine the solid-solution region for CTGS relative to its stoichiometric composition, and then to generate a phase diagram for CTGS at elevated temperatures so as to avoid the appearance of a secondary phase. A narrow solid-solution region usually indicates a highly ordered structure, as the locations of atoms are restricted to specific sites and thus a highly homogeneous bulk crystal is expected.

The phase diagrams of multi-component CTGS-type systems have not been well studied to date. In this work, therefore, we attempted to determine the boundary compositions at which CTGS coexists with secondary phases, by applying a lever rule to obtain the volume ratios of the secondary phases and the matrix CTGS phase, a process that consequently determined the solid-solution region for CTGS.

1.4 Purpose and overview of this thesis

The first purpose of this study was to investigate the locations of metal vacancies in CTGS crystal. The location of metal vacancy strongly influences the electrical resistivity of the bulk crystal at elevated temperatures.

The second aim, which is the main subject of this thesis, was to investigate the solid-solution region of CTGS to determine the growth conditions for CTGS crystal.

This thesis is arranged in five chapters:

Chapter 1 describes the background, purpose, and structure of the thesis. The electrical conduction mechanism and relation between the location of metal vacancies and the conductivity of langasite-type crystals are also presented.

In Chapter 2, eight possible crystal-site structures of CTGS are proposed by applying the Hume–Rothery rules and then narrowed down to three likely structures by determining the degrees of freedom in the crystal sites.

In Chapter 3, we determine the solid-solution region of CTGS by applying a lever rule to the data related to the compositions and proportions of the secondary phases coexisting with a CTGS matrix. The crystal-site structure of CTGS and the locations of metal vacancies are then revealed.

Chapter 4 discusses the liquid immiscibility that may result in the secondary phase during CTGS growth.

Chapter 5 presents a summary and the conclusions of the thesis.

Chapter 2 Crystal-site structure of langasite-type crystals

Because the electrical resistivity of langasite-type crystals is strongly affected by the presence of metal vacancy (V_M), we investigate the locations of metal vacancies in CTGS crystal. This chapter focuses on the crystal-site structure of CTGS, which eventually narrow down the three where the possible locations of the constituent elements are clarified.

2.1 Crystal-site structure

A crystal-site structure describes the possible locations of constituent elements and vacancies, as well as those of antisite defects. A crystal-site structure is discussed in association with its solid-solution region.

Hume–Rothery rules are used to reveal the possible pairs of solute and solvent elements. These rules govern the solid solution by considering the factors as follows [32]:

1. Atomic size factor: The atomic diameter of the solute atom differs from that of the solvent atom within a range of 15%. In such cases, the size factor is favorable for an extensive solid solution. In contrast, when the difference is greater than 15%, the solubility is limited.
2. Electrochemical effect: To form an extensive solid solution, a small electronegativity difference between the solute and solvent is favored. When the difference in electronegativity is large, the two elements are inclined to form compounds rather than solid solutions.
3. Relative valence effect: A higher-valence element is more likely to dissolve into a lower-valence element than the vice-versa case. When the solute and solvent elements have a same valence, they are likely to exhibit maximum solid solubility.
4. Structure of elements: To achieve high solubility over a wide composition range, the crystal structures and coordination numbers of the solute and solvent must be same.

The Hume–Rothery rules are used to predict the elements that will form a solid

solution in multi-component systems [32]; these elements are favored in the discussion of extensive solid solutions and will be used first to propose crystal-site structures in langasite-type crystals with four elements. However, the word “extensive” in the rules is not clearly defined. The rules provide a preliminary estimation of the crystal-site structure. Constraints must be employed to narrow down the possible crystal-site structures for a limited solid solution in a multi-component material.

The possible crystal-site structures are discussed in terms of the degrees of freedom in each site, which is equal to the difference in the number of elements in one site, # of parameter (# of para. hereafter)., minus the number of constraints, # of constraints (# of const. hereafter)., as illustrated in Eq. 2.1. The principles and details of the degrees of freedom in site have been discussed in reference [33]. The constraints applied to one site are as follows:

1. Mass conservation constraint: The sum of the ratio of all the elements in one site is equal to one. Notably, V_{m} is regarded as a type of element.
2. Charge balance constraint: V_{m} is formed to compensate the charge imbalance caused by an antisite defect.
3. Chemical potentials of a certain element are equal between sites (A, B, C, D), i.e., $\mu_A^i = \mu_B^i = \mu_C^i = \mu_D^i$, which is applied to all related chemical elements and to V_{m}:

$$\mathrm{F}(i) = \#\text{ of para.} - \#\text{ of const.} \geq 0, \ (i \text{ represents site A, B, C, or D}) \qquad (2.1)$$

A crystal can be formed only with a crystal-site structure that has non-negative degrees of freedom. In this study, we will apply degrees of freedom discussion to determine the crystal-site structure of langasite-type crystals.

2.2 Crystal-site structure of a langasite-type crystal with three elements

The model of the degrees of freedom introduced in Section 2.1 is applied to a langasite-type crystal with three elements. The consistency between the experimental results from previous work [34] and the obtained crystal-site structures in the present section demonstrate the validity of the model of the degrees of freedom.

Well-known and representative langasite-type crystals with three elements such as langatate (LTG, $La_3Ga_{5.5}Ta_{0.5}O_{14}$) and langasite (LGS, $La_3Ga_5SiO_{14}$) have been extensively investigated. The solid-solution regions of LTG and LGS have been reported by H. Kimura et al. [34] and S. Uda et al. [35], respectively. However, neither group of authors discussed the crystal-site structure of these materials.

In LTG, La^{3+} occupies the A site, whereas Ga^{3+} occupies C and D sites and half of the B site. Two crystal-site structures with metal vacancy locations at the A site (V_A model) and B site (V_B model) are possible, as shown in Fig. 2.1.

In the V_A model, as shown in Fig. 2.1 and Table 2.1, La^{3+} and V_M shares the A site, which makes the # of para. of the A site equal to 2, whereas the constraints of the A site are mass conservation and charge balance, which makes the # of const. in the A site also equal to 2. Therefore, the degrees of freedom in the A site equals to 0. Ta^{5+} and Ga^{3+} share the B site, which makes the # of para. of the B site equal to 2, whereas the constraints of the B site are mass conservation and chemical potential equilibrium of Ga^{3+} between B, C and D sites, which makes the # of const. in the B site equal to 2. Therefore, the degrees of freedom in the B site is also equal to 0. C and D sites are occupied only by Ga^{3+}, and the equality of the chemical potential of Ga^{3+} between B, C and D sites is the only constraint in both sites. Therefore, the degrees of freedom in C and D sites is equal to 0. Thus, in the case of the crystal-site structure of the V_A model in LTG, each degrees of freedom of the four sites is equal to 0, which makes the V_A model a viable crystal-site structure.

We applied a similar evaluation to the crystal-site structure of the V_B model in LTG; the results are presented in Table 2.1. La^{3+} occupies the A site, which makes the # of para. of the A site equal to 1, and the A site has no constraints. Thus, the degrees of freedom of the A site is equal to 1. Ta^{5+}, Ga^{3+}, and V_M share the B site, which makes the # of para. of the B site equal to 3; the constraints of the B site are mass

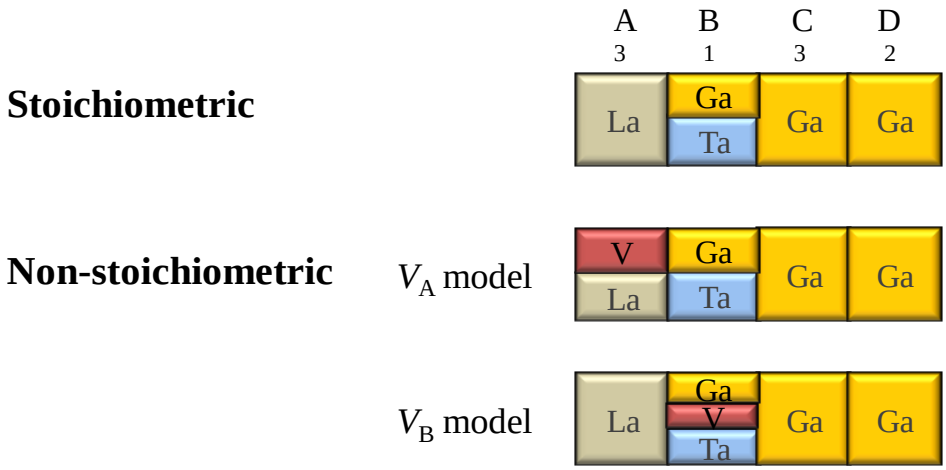

Fig. 2.1 Schematic of the crystal-site structures in LTG.

Table 2.1 Degrees of freedom in each site for the V_A and V_B models of LTG.

V_A model	Site			
	A	**B**	**C**	**D**
Elements	La, V	Ta, Ga,	Ga	Ga
#(para.)	2	2	1	1
Constraints	·Mass conservation ·Charge balance	·Mass conservation · $\mu^{Ga}_{C-site} = \mu^{Ga}_{B-site}$	· $\mu^{Ga}_{C-site} = \mu^{Ga}_{B-site}$	$\mu^{Ga}_{C-site} = \mu^{Ga}_{D-site}$
#(cons.)	2	2	1	1
F(i)	**0**	**0**	**0**	**0**

V_B model	Site			
	A	**B**	**C**	**D**
Elements	La	Ta, Ga, V	Ga	Ga
#(para.)	1	3	1	1
Constraints	None	·Mass conservation ·Charge balance · $\mu^{Ga}_{C-site} = \mu^{Ga}_{B-site}$	· $\mu^{Ga}_{C-site} = \mu^{Ga}_{B-site}$	$\mu^{Ga}_{C-site} = \mu^{Ga}_{D-site}$
#(cons.)	0	3	1	1
F(i)	**1**	**0**	**0**	**0**

conservation, charge balance, and chemical potential equality of Ga^{3+} among B, C, and D sites, which makes the # of const. in the B site equal to 3. Therefore, the degrees of freedom of the B site is equal to 0. C and D sites are occupied only by Ga^{3+}, and the equality of the chemical potential of Ga^{3+} between C and D sites is the only constraint in both sites. Thus, the degrees of freedom of C and D sites is equal to 0. In the crystal-site structure of the V_B model of LTG, the degrees of freedom for all four sites is equal to 0, which makes the V_B model a viable crystal-site structure.

The knowledge of the occupancy of La^{3+}, Ta^{5+}, and Ga^{3+} in each site allows us to assess the solid-solution region of the V_A and V_B models. Compared with the stoichiometric composition, the composition of the V_A model is La^{3+}- and Ga^{3+}-deficient in A and B sites, respectively, and is Ta^{5+}-rich in the B site. In contrast, in the V_B model, La^{3+} fills the A site, and the B site is Ga-deficient and Ta-rich. The presumed solid-solution regions of the V_A and V_B models are schematically presented for the system La_2O_3–Ga_2O_3–Ta_2O_5 (Fig. 2.2 (a)). The presumed solid-solution region is consistent with the experimental results reported by H. Kimura et al. [34] (presented in this study in Fig. 2.2 (b)), which indicates the validity the of the predicted crystal-site structure.

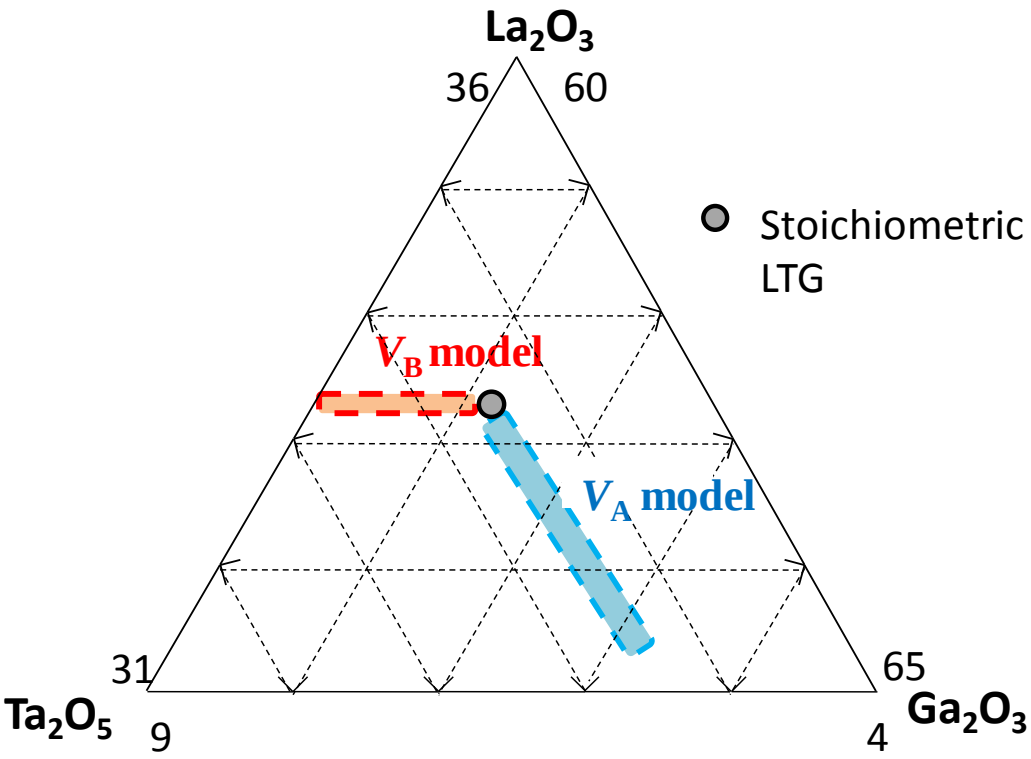

(a)

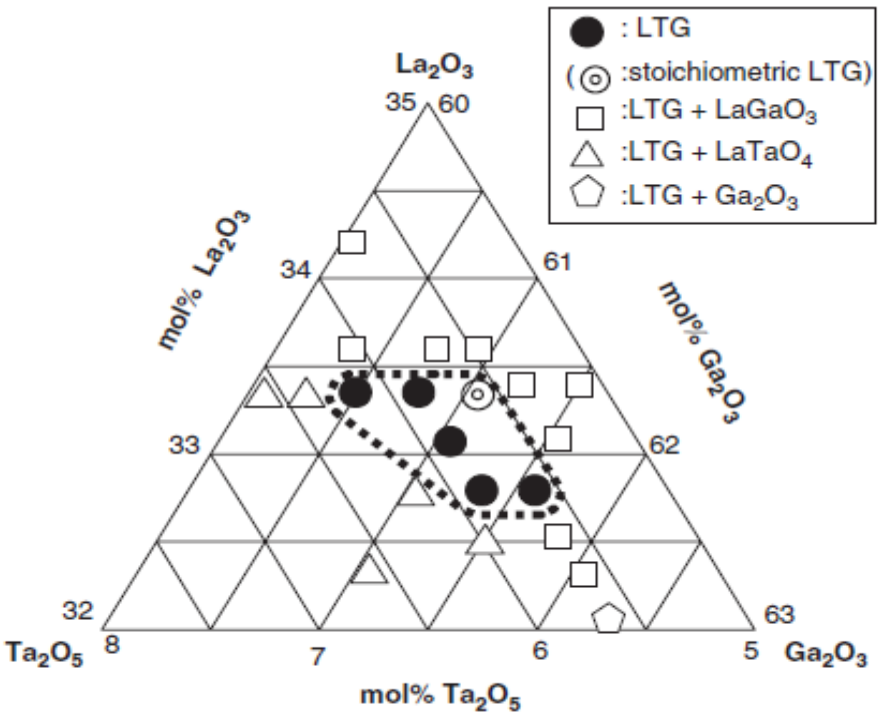

(b)

Fig. 2.2 Solid-solution region of LTG. (a) Presumed solid-solution regions of the crystal-site structures of the V_A and V_B models. (b) Solid-solution region of LTG determined by the X-ray diffraction (XRD) method and reported in Ref. [34].

2.3 Crystal-site structure of a langasite-type crystal with four elements

In a langasite-type crystal with four elements, the possible elements for each of four sites are Ca^{2+}, Sr^{2+}, and Ba^{2+} for the A site; Ta^{5+} and Nb^{5+} for the B site; Ga^{3+}, Al^{3+}, and Fe^{3+} for the C site; and Si^{4+} and Ge^{4+} for the D site. More than 200 four-element langasite-type crystals have been reported previously [11]. The crystal-site structures of langasite-type crystals with four elements are specific to their constituent elements. This section focuses on the crystal-site structure of CTGS. The discussion here is applicable to other langasite-type crystals with four elements.

Hume–Rothery rules will be applied in the discussion of the crystal-site structure. Table 2.2 [36] presents the radius, electronegativities, coordination numbers, and the valence of Ca, Ta, Ga, and Si.

The coordination numbers of Ca^{2+}, Ta^{5+}, and Si^{4+} are 8, 6, and 4, respectively. The coordination number of Ga^{3+} is 4 or 6. Thus, the decahedral A site can accommodate only Ca^{2+}, whereas the octahedral B site can accommodate Ta^{5+} and Ga^{3+}, and the tetrahedral C and D sites can accommodate Ga^{3+} and Si^{4+}. These restrictions lead to a prediction that a solid solution will have the B site occupied by Ta^{5+} and Ga^{3+} and C and D sites occupied by Ga^{3+} and Si^{4+}; thus, the candidate elements are as outlined in Table 2.3. The difference in radius (ΔR) between the solute and solvent elements was calculated using Eq. 2.2. The $\Delta R^{\mathrm{B}}_{(\mathrm{Ga,Ta})}$, $\Delta R^{\mathrm{C}}_{(\mathrm{Ga,Si})}$, and $\Delta R^{\mathrm{D}}_{(\mathrm{Si,Ga})}$ were calculated to be 3.1 %, 44.6 %, and 80.7 %, respectively. This result demonstrates that very limited solid solution exists in a composition range between Ga and Si in the D site.

$$\Delta R_{(\mathrm{Solute,Solvent})} = \left| \frac{R_{\mathrm{Solute}} - R_{\mathrm{Solvent}}}{R_{\mathrm{Solvent}}} \right| \times 100\% \qquad (2.2)$$

To compensate the charge imbalance caused by the incorporation of antisite defects, a metal vacancy is formed in the site. On the basis of the incorporation of intrinsic elements, antisite defects, and metal vacancies, eight crystal-site structures were proposed for CTGS using the Hume–Rothery rules (shown in Fig. 2.3); they are identified as models ***1***–***8***. Model ***1*** contains no metal vacancies, whereas models ***2***–***8*** contain vacancies at one of the four sites. As denoted in Section 2.1, the

Table 2.2 Ionic radii of elements used in this thesis according to coordination number [36].

Element (Coord.#)	Ionic Radius (Å)	Electro-negativitiy	Valence	Site & Coord.#
Ca (8)	1.12	1.0	+2	A (8)
Ta (6)	0.64	1.5	+5	B (6)
Ga (4,6)	0.47, 0.62	1.81	+3	C (4)
Si (4)	0.26	1.9	+4	D (4)

Table 2.3 Possible candidate elements for sites A, B, C, and D.

Site	Possible Candidates
A	Ca
B	Ta, Ga
C	Ga, Si
D	Si

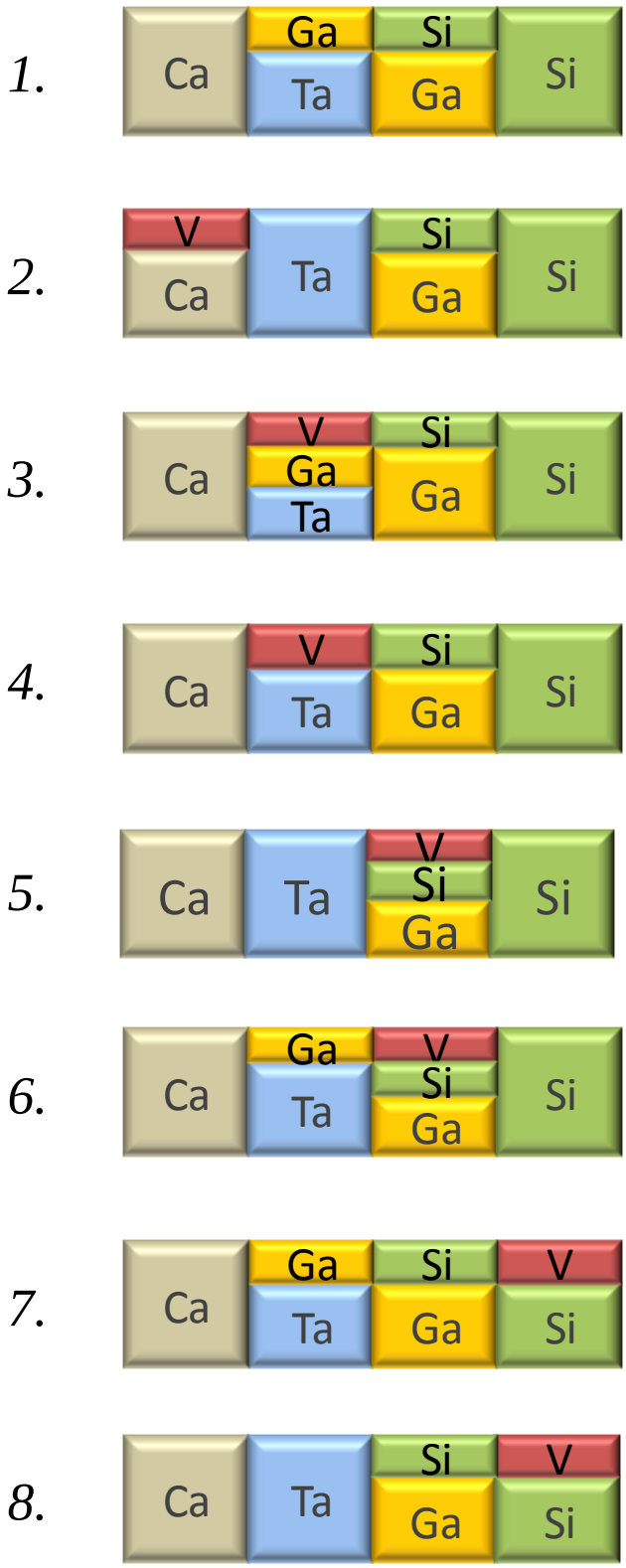

Fig. 2.3 Schematic of the crystal-site structures of models ***1***–***8*** in CTGS.

Hume–Rothery rules do not sufficiently narrow down the range of possible crystal-site structures. The discussion based on the similar degrees of freedom in Section 2.2 also applies to the degrees of freedom in each site of the 8 possible CTGS models.

The # of para., the number of constraints (# of cons.), and the degrees of freedom ($F(i)$) in each of the four sites in models ***1***–***8*** are listed in Table 2.4.

In model ***1*** (Table 2.4 (a)), Ca^{2+} completely occupies the A site, which makes the # of para. of the A site equal to 1 with no constraints. Therefore, the degrees of freedom of the A site is equal to 1. Ta^{5+} and Ga^{3+} share the B site, which makes the # of para. of the B site equal to 2. The constraints of the B site are mass conservation, charge balance, and chemical potential equilibrium of Ga^{3+} between sites B and C; thus, the # of cons. of the B site is equal to 3. Consequently, the degrees of freedom of the B site is equal to −1. Ga^{3+} and Si^{4+} share the C site, which makes # of para. of the C site equal to 2. The constraints of the C site are mass conservation, chemical potential equality of Ga^{3+} between B and C sites, and the chemical potential equality of Si^{4+} between C and D sites. The # of cons. of the C site is therefore equal to 3. Consequently, the degrees of freedom of the C site is equal to −1. The D site is completely occupied only by Si^{4+}, and the chemical potential equality of Ga^{3+} is the only constraint in the D site. Therefore, the degrees of freedom of the D site is equal to 0. Because the degrees of freedom of B and C sites are negative, the crystal-site structure of model ***1*** is excluded.

In model ***2*** (Table 2.4 (b)), vacancies and Ca^{2+} share the A site, which makes the # of para. of the A site equal to 2. The constraints of the A site are mass conservation and charge balance. Therefore, the degrees of freedom of the A site is equal to 0. Ta^{5+} completely occupies the B site, which makes the # of para. of the B site equal to 1, and the B site has no constraints. Therefore, the degrees of freedom of the B site is equal to 1. Ga^{3+} and Si^{4+} share the C site, which makes the # of para. of the C site equal to 2. The constraints of the C site are mass conservation and chemical potential equality of Si^{4+} between C and D sites. The # of cons. of the C site is equal to 2. Therefore, the degrees of freedom of the C site is equal to 0. The D site is completely occupied only by Si^{4+}, and the chemical potential equality of Ga^{3+} is the only constraint in the D site. Therefore, the degrees of freedom of the D site is equal to 0. Because the degrees of freedom of all sites are non-negative, the crystal-site structure of model ***2*** is confirmed to be viable.

Table 2.4 Degrees of freedom in site for models ***1***–***3*** of CTGS. Tables a–c correspond to models ***1***–***3***, respectively.

(a) Model ***1***

Model *1*	A	B	C	D
Elements	Ca	Ta, Ga	Ga, Si	Si
#(para.)	1	2	2	1
Constraints	· None	· Mass conservation · Charge balance $\cdot \mu_{C-site}^{Ga} = \mu_{B-site}^{Ga}$	· Mass conservation $\cdot \mu_{C-site}^{Si} = \mu_{D-site}^{Si}$ $\cdot \mu_{C-site}^{Ga} = \mu_{B-site}^{Ga}$	$\cdot \mu_{C-site}^{Si} = \mu_{D-site}^{Si}$
#.(cons.)	0	3	3	1
F(i)	**1**	**-1**	**-1**	**0**

(b) Model ***2***

Model *2*	A	B	C	D
Elements	Ca, *V*	Ta	Ga, Si	Si
#(para.)	2	1	2	1
Constraints	·Mass conservation ·Charge balance	· None	·Mass conservation $\cdot \mu_{C-site}^{Si} = \mu_{D-site}^{Si}$	$\cdot \mu_{C-site}^{Si} = \mu_{D-site}^{Si}$
#.(cons.)	2	0	2	1
F(i)	**0**	**1**	**0**	**0**

(c) Model ***3***

Model *3*	A	B	C	D
Elements	Ca	*V*, Ta, Ga	Ga, Si	Si
# of para.	1	3	2	1
Constraints	· None	· Mass conservation $\cdot \mu_{C-site}^{Ga} = \mu_{B-site}^{Ga}$ ·Charge balance	· Mass conservation $\cdot \mu_{C-site}^{Ga} = \mu_{B-site}^{Ga}$ $\cdot \mu_{C-site}^{Ga} = \mu_{B-site}^{Ga}$	$\cdot \mu_{C-site}^{Si} = \mu_{D-site}^{Si}$
# of const.	0	3	3	1
F	**1**	**0**	**-1**	**0**

In model ***3*** (Table 2.4 (c)), Ca^{2+} completely occupies the A site, which makes the # of para. of the A site equal to 1, and the A site has no constraints. Thus, the degrees of freedom of the A site is equal to 1. Vacancies, Ta^{5+}, and Ga^{3+} share the B site, which makes the # of para. of the B site equal to 3. The constraints of the B site are mass conservation, charge balance, and chemical potential equality of Ga^{3+} between B and C sites, which makes the # of const. of the B site equal to 3. Therefore, the degrees of freedom of the B site is equal to 0. Ga^{3+} and Si^{4+} share the C site, which makes the # of para. of the C site equal to 2. The constraints of the C site are mass conservation, chemical potential equality of Ga^{3+} between B and C sites, and chemical potential equality of Si^{4+} between C and D sites. The # of cons. of the C site is therefore 3. Thus, the degrees of freedom of the B site is equal to −1. The D site is completely occupied only by Si^{4+}, and the chemical potential equality of Ga^{3+} between C and D sites is the only constraint for the D site. Therefore, the degrees of freedom of the D site is equal to 0. Because the degrees of freedom of C site is −1, the crystal-site structure of model ***3*** is excluded.

In model ***4*** (Table 2.4 (d)), Ca^{2+} completely occupies the A site, which makes the # of para. of the A site equal to 1, and the A site has no constraints. Therefore, the degrees of freedom of the A site is equal to 1. The vacancies and Ta^{5+} share the B site, which makes the # of para. of the B site equal to 2; the constraints of the B site are mass conservation and charge balance, which makes the # of const. of the B site equal to 2. Thus, the degrees of freedom of the B site is equal to 0. Ga^{3+} and Si^{4+} share the C site, which makes the # of para. of the C site equal to 2. The constraints of the C site are mass conservation and chemical potential equality of Si^{4+} between C and D sites. The # of cons. of the C site is therefore equal to 2. Thus, the degrees of freedom of the B site is equal to 0. The D site is completely occupied only by Si^{4+}, the chemical potential equality of Ga^{3+} between C and D sites is the only constraint in the D site. Thus, the degrees of freedom of the D site is equal to 0. Because the degrees of freedom of all sites are non-negative, the crystal-site structure of model ***4*** is confirmed to be viable.

In model ***5*** (Table 2.4 (e)), Ca^{2+} and Ta^{5+} completely occupy A and B sites, respectively, which makes the # of para. of A and B sites equal to 1, and these sites have no constraints. The degrees of freedom of A and B sites are therefore equal to 1. Vacancies, Ga^{3+}, and Si^{4+} share the C site, which makes the # of para. of the C site equal to 3. The constraints of the C site are mass conservation, charge balance, and

chemical potential equality of Si^{4+} between C and D sites, which makes the # of cons. of the C site equal to 3. Thus, the degrees of freedom of the C site is equal to 0. The site D is completely occupied only by Si^{4+}, and the chemical potential equality of Ga^{3+} is the only constraint in the D site. Thus, the degrees of freedom of the D site is equal to 0. Because the degrees of freedom of all sites are non-negative, the crystal-site structure of model ***5*** is confirmed to be viable.

In model ***6*** (Table 2.4 (f)), Ca^{2+} completely occupies the A site, which makes the # of para. of the A site equal to 1, and the A site has no constraints. Therefore, the degrees of freedom of the A site is equal to 1. Ta^{5+} and Ga^{3+} share the B site, which makes the # of para. of the B site equal to 2. The constraints of the B site are mass conservation and chemical potential equality of Ga^{3+} between B and C sites. The # of cons. of the B site is therefore equal to 2. Thus, the degrees of freedom of the B site is 0. Vacancies, Ga^{3+}, and Si^{4+} share the C site, which makes the # of para. of the C site equal to 3. The constraints of the C site are mass conservation, charge balance, chemical potential equality of Ga^{3+} between B and C sites, and the chemical potential equality of Si^{4+} between C and D sites, which makes the # of cons. of the C site equal to 4. Thus, the degrees of freedom of the B site is equal to −1. The D site is completely occupied only by Si^{4+}, and the chemical potential equality of Ga^{3+} between C and D sites is the only constraint. Therefore, the degrees of freedom of the D site equals to 0. Because the degrees of freedom of the C site is −1, the crystal-site structure of model ***6*** is excluded.

Table 2.4 Degrees of freedom in site for models ***4***–***6*** of CTGS. Tables d–f correspond to models ***4***–***6***, respectively.

(d) Model ***4***

Model *4*	A	B	C	D
Elements	Ca	*V*, Ta	Ga, Si	Si
#(para.)	1	2	2	1
Constraints	· None	· Mass conservation ·Charge balance	· Mass conservation · $\mu_{C-site}^{Si} = \mu_{D-site}^{Si}$	· $\mu_{C-site}^{Si} = \mu_{D-site}^{Si}$
#.(cons.)	0	2	2	1
F(i)	**1**	**0**	**0**	**0**

(e) Model ***5***

Model *5*	A	B	C	D
Elements	Ca	Ta	*V*, Ga, Si	Si
#(para.)	1	1	3	1
Constraints	· None	· None	·Mass conservation · $\mu_{C-site}^{Ga} = \mu_{B-site}^{Ga}$ ·Charge balance	· $\mu_{C-site}^{Si} = \mu_{D-site}^{Si}$
#.(cons.)	0	0	3	1
F(i)	**1**	**1**	**0**	**0**

(f) Model ***6***

Model *6*	A	B	C	D
Elements	Ca	Ta, Ga	*V*, Ga, Si	Si
# of para.	1	2	3	1
Constraints	· None	· Mass conservation · $\mu_{C-site}^{Ga} = \mu_{B-site}^{Ga}$	·Mass conservation · Charge balance · $\mu_{C-site}^{Ga} = \mu_{B-site}^{Ga}$ · $\mu_{C-site}^{Si} = \mu_{D-site}^{Si}$	· $\mu_{C-site}^{Si} = \mu_{D-site}^{Si}$
# of const.	0	2	4	1
F	**1**	**0**	**-1**	**0**

In model ***7*** (Table 2.4 (g)), Ca^{2+} completely occupies the A site, which makes the # of para. of the A site equal to 1, and the A site has no constraints. Thus, the degrees of freedom of the A site is equal to 1. Ta^{5+} and Ga^{3+} share the B site, which makes the # of para. of the B site equal to 2. The constraints of the B site are mass conservation and chemical potential equality of Ga^{3+} between B and C sites. The # of cons. of the B site is therefore equal to 2. Thus the degrees of freedom of the B site is 0. Ga^{3+} and Si^{4+} share the C site, which makes the # of para. of the C site equal to 2. The constraints of the C site are mass conservation, chemical potential equality of Ga^{3+} between B and C sites, and the chemical potential equality of Si^{4+} between C and D sites, which makes the # of cons. of the C site equal to 3. Therefore, the degrees of freedom of the C site is equal to −1. The D site is shared by vacancies and Si^{4+}, which makes the # of para. of the D site equal to 2. The constraints of the D site are mass conservation, charge balance, and chemical potential equality of Si^{4+} between C and D sites. The # of cons. of the D site is therefore equal to 3. Consequently, the degrees of freedom of the D site is equal to −1. Because the degrees of freedom of C and D sites is equal to −1, the crystal-site structure of model ***7*** is excluded.

In model ***8*** (Table 2.4 (h)), Ca^{2+} and Ta^{5+} completely occupy A and B sites, respectively, which makes the # of para. of A and B sites equal to 1, both A and B sites have no constraints. The degrees of freedom of A and B sites is equal to 1. Ga^{3+} and Si^{4+} share the C site, which makes the # of para. of the B site equal to 2. The constraints of the C site are mass conservation and chemical potential equality of Si^{4+} between C and D sites, which makes the # of cons. of the C site equal to 2. Thus, the degrees of freedom of the C site equals to 0. The D site accommodates vacancies and Si^{4+} and has the constraints of mass conservation, charge balance, and the chemical potential equality of Si^{4+} in C and D sites. Thus, the degrees of freedom of the D site is equal to −1, and therefore, the crystal-site structure of model ***8*** is excluded.

To conclude the above discussion, the crystal-site structures of models ***2***, ***4***, and ***5*** shown in Fig. 2.3 and Table 2.4 have non-negative degrees of freedom for each of the four sites. Thus, they are confirmed to be viable in CTGS. This result shows that metal vacancies will not be located at the D site. Metal vacancies in models ***2***, ***4***, and ***5*** are located in A, B, and C sites, respectively, and models V_A, V_B, and V_C will be used to respectively address them hereafter.

Table 2.4 Degrees of freedom in site for models ***7***–***8*** of CTGS. Tables g–h correspond to models ***7***–***8***, respectively.

(g) Model ***7***

Model *7*	**A**	**B**	**C**	**D**
Elements	Ca	Ta, Ga	Ga, Si	***V***, Si
#(para.)	1	2	2	2
Constraints	· None	· Mass conservation · $\mu_{C-site}^{Ga} = \mu_{B-site}^{Ga}$	· Mass conservation · $\mu_{C-site}^{Ga} = \mu_{B-site}^{Ga}$ · $\mu_{C-site}^{Si} = \mu_{D-site}^{Si}$	·Mass conservation ·Charge balance · $\mu_{C-site}^{Si} = \mu_{D-site}^{Si}$
#.(cons.)	0	2	3	3
F(i)	**1**	**0**	**-1**	**-1**

(h) Model ***8***

Model *8*	**A**	**B**	**C**	**D**
Elements	Ca	Ta	Ga, Si	***V***, Si
# of para.	1	1	2	2
Constraints	· None	· None	·Mass conservation · $\mu_{C-site}^{Si} = \mu_{D-site}^{Si}$	·Mass conservation ·Charge balance ·$\mu_{C-site}^{Si} = \mu_{D-site}^{Si}$
# of const.	0	0	2	3
F	**1**	**1**	**0**	**-1**

2.4 Summary

The crystal-site structure describes the locations of intrinsic elements, antisite defects, and metal vacancies. This chapter introduces the Hume–Rothery rules and the model of the degrees of freedom in site to narrow down the possible crystal-site structures associated with the solid solution among the constituent elements of Ca, Ta, Ga, and Si.

The Hume–Rothery rules govern the primary substitution solid solution and are used to propose crystal-site structures in certain compositions of crystals. The proposed crystal-site structures are further narrowed down by the model of degrees of freedom in site, which is evaluated by the difference in the number of elements in one site, # of para., minus the number of constraints, # of cons. The crystal-site structure is possible only when the degrees of freedom for each of the four sites is non-negative. They are V_A, V_B and V_C crystal-site structures where the metal vacancy is located in A, B and C sites, respectively.

Chapter 3 Solid-solution region for a CTGS crystal

The study of the solid-solution region of a compound is important from both the scientific and technological view points of crystal growth. A narrow solid-solution region usually accompanies a highly ordered structure because atoms are restricted to specific sites; thus, a highly homogeneous bulk crystal is expected. The solid-solution region characterizes the composition shift from the stoichiometric composition of a crystal, which reveals the sites of vacancies and anti-site defects, as denoted in Section 2.1. Possible crystal-site structures of the V_A, V_B, and V_C models that have metal vacancies in sites A, B, and C, respectively, have been proposed on the basis of crystal-site structures, as discussed in Section 2.3. The model that is suitable will be determined based on examinations of the solid-solution region of CTGS. Unlike langasite-type crystals with three elements, no study on the solid-solution region of langasite-type crystals with four elements has been previously reported. In this chapter, we investigate the solid-solution region of CTGS and discuss which of the three possible crystal-site structures of CTGS are valid.

3.1 Experimental

3.1.1 Initial bulk composition

In the quaternary CaO-Ta_2O_5-Ga_2O_3-SiO_2 system (Fig. 3.1 (a)), stoichiometric CTGS (s-CTGS) locates on the CaO equi-concentration plane (Fig. 3.1 (b)), where Ca/(Ca+Ta+Ga+Si) = 1/3. The compositions of the prepared samples used in all experimental trials were located on this plane, which hereafter will be referred as the CaO-1/3 plane. Three compositional series around the stoichiometric point were examined on the CaO-1/3 plane in the pseudo-ternary system: Series I, in which CaO and Ta_2O_5 were constant while Ga_2O_3 and SiO_2 were variable; Series II, in which CaO and SiO_2 were constant while Ga_2O_3 and Ta_2O_5 were variable; and Series III, in which CaO and Ga_2O_3 were constant while SiO_2 and Ta_2O_5 were variable (Fig. 3.1 (c)).

Employing the CaO-1/3 plane allowed us to assume that the concentration of the CaO component was constant for all three series, since Ca occupies the largest

dodecahedral site (the A site) and no other elements in CTGS would have replaced Ca at this site. This assumption is supported by the observation that the secondary phases that we investigated around the s-CTGS composition always exhibited the same Ca molar ratio: Ca/(Ca+Ta+Ga+Si) = 1/3. A pair of compositions was chosen for study from each of the three series, as shown in Fig. 3.1 (c): I (a) and (b), II (c) and (d), and III (e) and (f), and their compositions are listed in Table 3.1.

Table 3.1 Initial bulk compositions of samples (s) and (a)-(f).

		Ca/(Ca+Ta+Ga+Si)=1/3		
	Sample	Ta/(Ta+Ga+Si) (%)	Ga/(Ta+Ga+Si) (%)	Si/(Ta+Ga+Si) (%)
Stoichiometric	(s)	16.67	50.00	33.33
Series I	(a)	16.67	51.25	32.08
	(b)	16.67	48.33	35.00
Series II	(c)	16.00	50.67	33.33
	(d)	18.00	48.67	33.33
Series III	(e)	17.25	50.00	32.75
	(f)	16.00	50.00	34.00

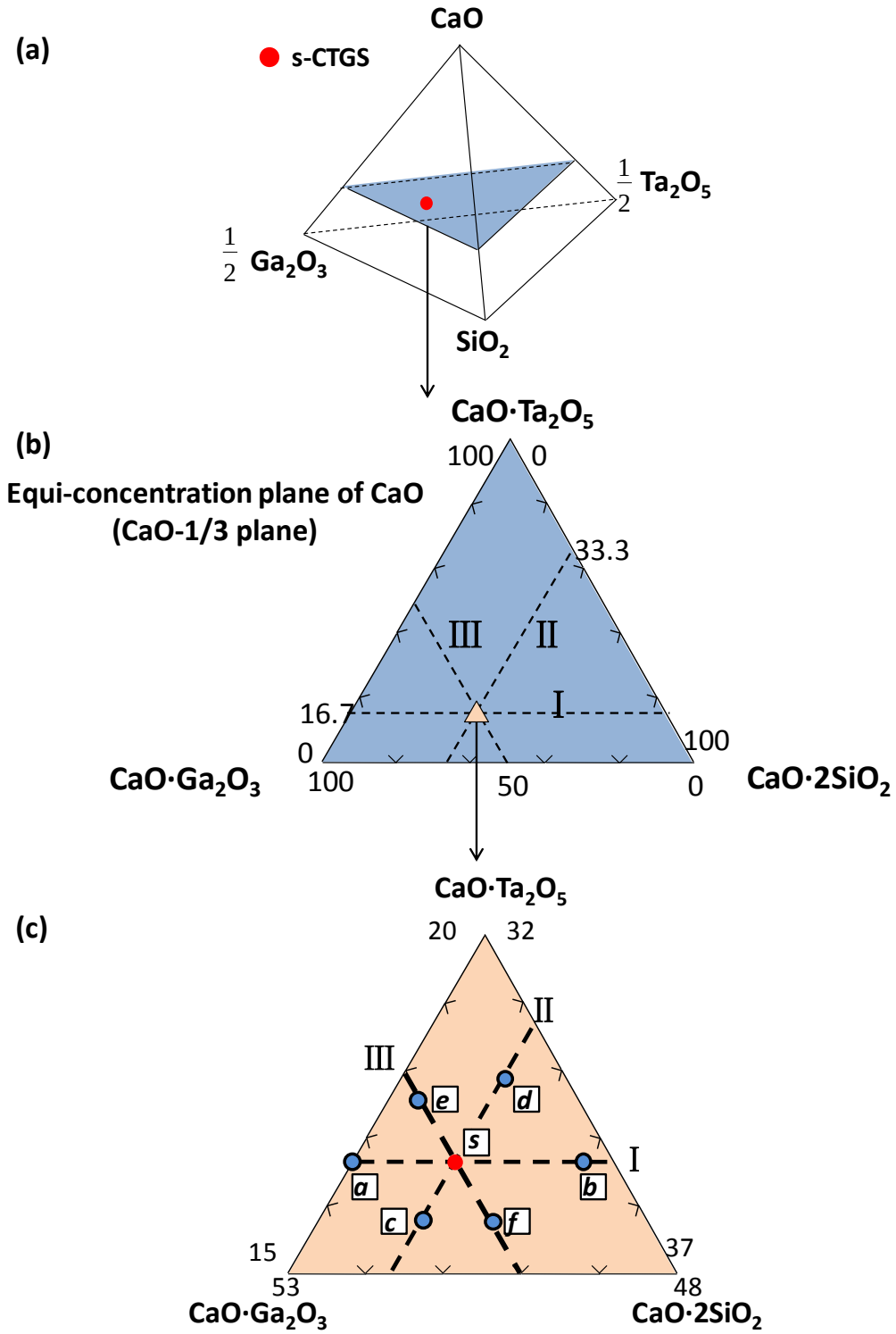

Fig. 3.1(a) schematic of quaternary CaO-Ta_2O_5-Ga_2O_3-SiO_2 system; (b) schematic of equi-concentration plane of CaO (CaO-1/3 plane); (c) initial bulk composition of Series I, II and III on the Ca-1/3 plane.

3.1.2 XRD analyses and backscattered electron image (BEI) observations

Chapter 3 focuses on the determination of the solid-solution region in the sintered CTGS with various initial compositions. XRD analyses and BEI observations are used to determine the solid-solution region in this study.

In XRD analyses, sintered CTGS was characterized by powder XRD; the powder patterns were collected using a Rigaku Ultima IV diffractometer equipped with a Cu-K_α target ($CuK_{\alpha1}$:$CuK_{\alpha2}$ = 2:1, λ = 0.15418 nm). Powdered α-Al_2O_3 was mixed with the samples as a reference. The XRD patterns were analyzed in the range of 20 °–60 ° using the 2θ–θ method; the X-ray tube was operated at 40 kV and 30 mA. The scan speed was 1 °per min with a step interval of 0.0002 °.

To observe the surface of the samples and measure the chemical compositions of the sintered materials of CTGS, BEIs were collected, and electron probe microanalysis (EPMA) was performed using a JEOL JSM 6610A system. Samples were embedded in resin and mirror polished for BEI observation. The compositions of existing phases were ascertained by EPMA, and the proportion of each phase was determined using the image processing software associated with the BEI measurement system.

3.1.3 Evaluation of the degrees of sintering

The starting materials, $CaCO_3$, Ta_2O_5, Ga_2O_3 and SiO_2, were all 99.99% pure. The raw Ta_2O_5, Ga_2O_3 and SiO_2 powders were pre-dried at 1100 ℃ and then mixed in the desired proportions. The mixed samples were subsequently ground and sintered at 1320 ℃ for 12 hours. The sintering process was repeated a total of four times to ensure that chemical equilibrium was achieved. Extensive sintering of these samples was necessary and the degree of sintering in each specimen was evaluated by the evolution of grain growth.

Densification was considered to be complete when the grain size plateaued, indicating an equilibrium state of mass transportation by diffusion [37,38]. For this purpose, the changes in grain size of s-CTGS after sintering for 12, 24, 36 and 48 h were examined. The grain size was calculated using the Scherrer equation (Eq. 3.1). The XRD patterns of s-CTGS were measured after the samples were sintered for 12,

24, 36, and 48 h (Fig. 3.2 (a)). The strongest peak 201, which was centered at 31.2 °, was used to analyze the change in grain size (shown in Fig. 3.2 (b), where the arrow indicates the half-maximum of the peaks). The full width at half maximum (FWHM) of the 201 peak is shown in Fig. 3.3. Parameter $k\lambda$ in Eq. 3.1 is equal to 0.15418 nm.

$$\text{Grain size (nm)} = \frac{k\lambda}{FWHM \times \cos\theta} \tag{3.1}$$

The grain size increased to 23 nm in the case of the sample sintered for 36 h (Fig. 3.4). The saturation of grain size indicates that the material transport at high temperatures achieves an equilibrium state. Thus, s-CTGS was thoroughly sintered. Consequently, all the samples in this study were sintered for 48 h.

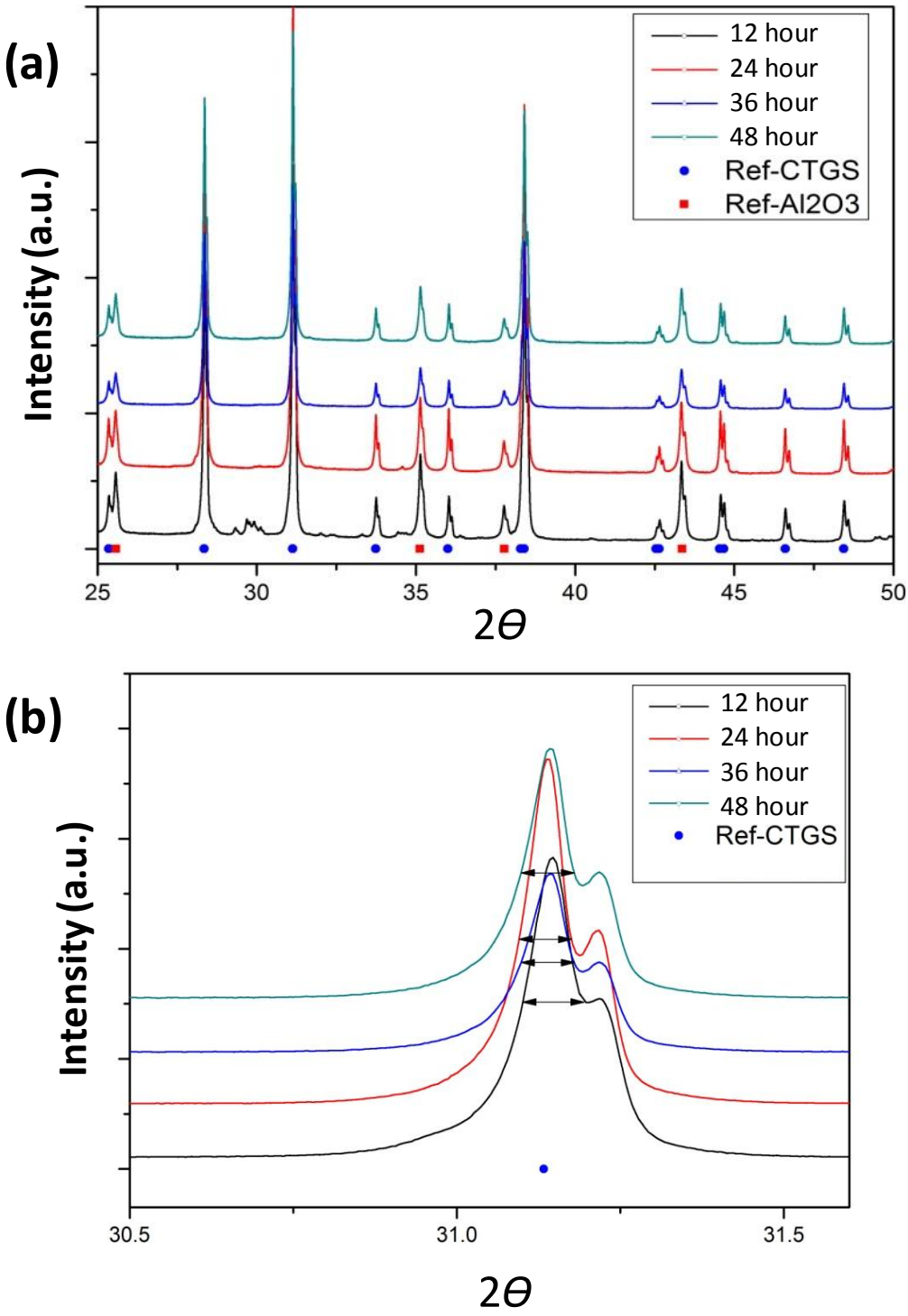

Fig. 3.2 XRD patterns of s-CTGS sintered at 1320 ℃ for 12 h, 24 h, 36 h, and 48 h: (a) the range from 25 °to 50 °and (b) the range from 30.5 °to 31.7 °.

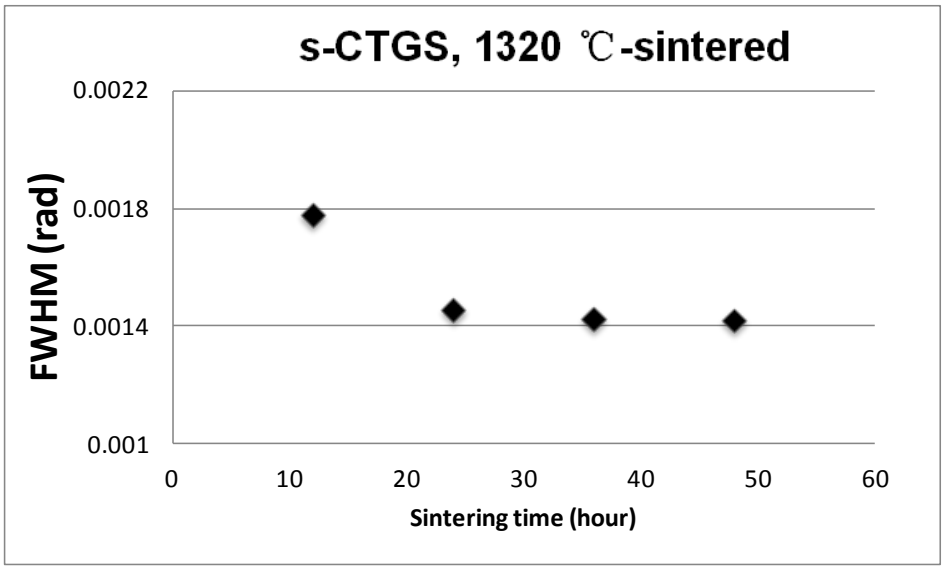

Fig. 3.3 Change in the FWHM of the 201 XRD peak as a function of sintering time.

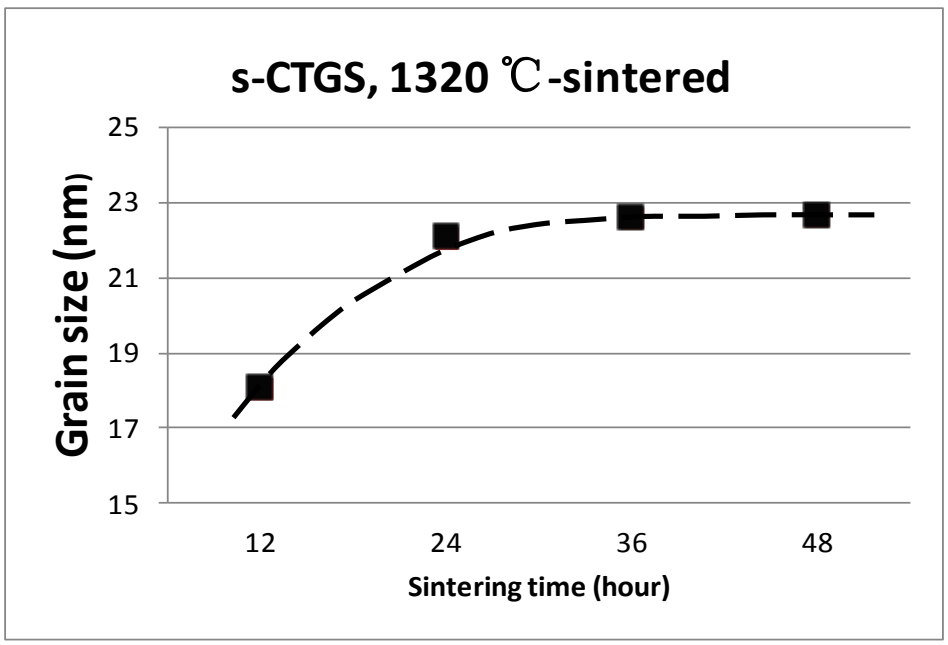

Fig. 3.4 Change in grain size estimated using Eq. 3.1 for the CTGS phase as a function of sintering time.

3.2 Secondary phase identification via XRD analysis

XRD analysis is a common means of determining the solid-solution region for oxide materials, including crystals in the langasite family. In Fig. 3.5, sample (s) represents a s-CTGS composition. There was no recognizable secondary phase in this sample since all peaks could be ascribed to CTGS, with the exception of peaks originating from Al_2O_3. On the other hand, samples from (a) to (f) were non-stoichiometric. As noted, samples (a) and (b), (c) and (d), and (e) and (f) belong to Series I, II and III, respectively, as illustrated in Fig. 3.1 (c). Fig. 3.5 presents the XRD reflection peaks of these samples. Sample (a), which was Ga-rich relative to the s-CTGS composition, generated peaks attributable to $Ca_3Ta_2Ga_4O_{14}$ (CTG), while samples (b) and (d), which were Ga-poor, produced peaks due to $CaTa_2O_6$ (CT2). Sample (c) did not show any secondary peaks. In each case, the intensities of the secondary phase reflection peaks were not strong enough to allow quantitative analysis, and thus XRD data were insufficient to determine the solid-solution region for CTGS. Based on these results, we therefore applied a lever rule to examine the proportions of secondary phases, based on BEI observations combined with EPMA analysis.

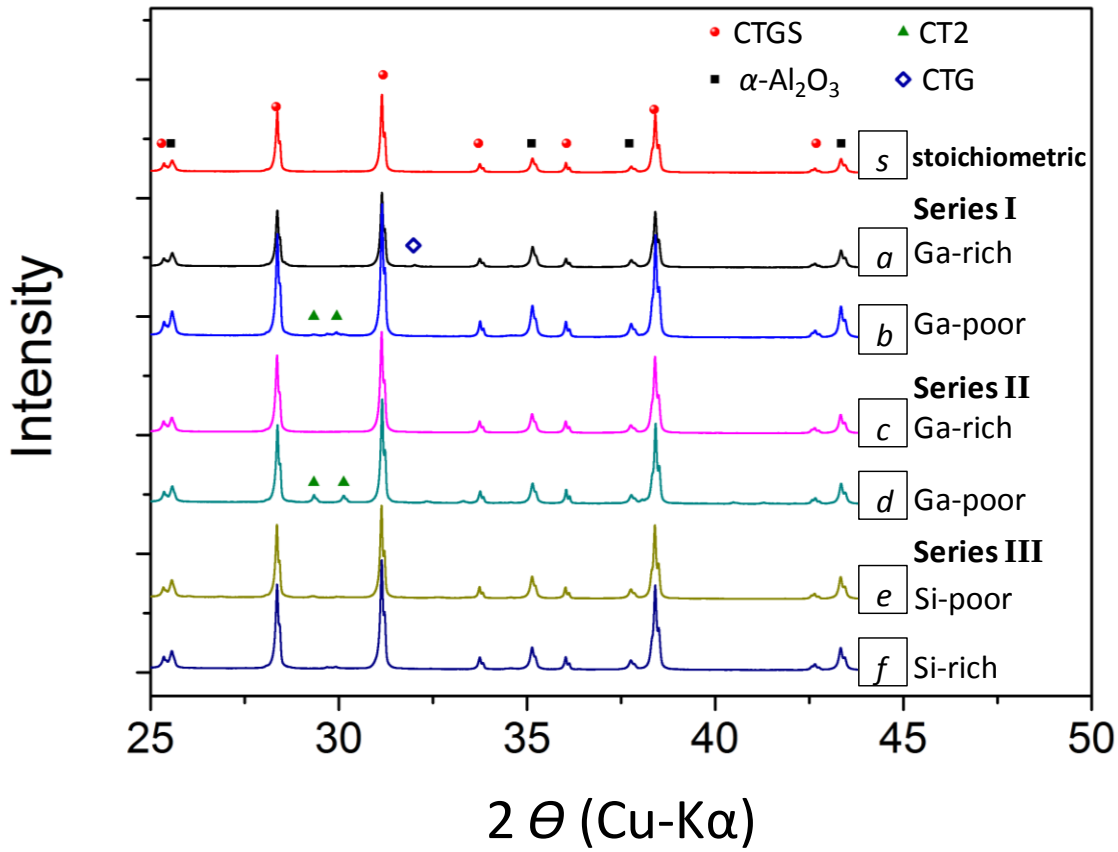

Fig. 3.5 X-ray diffraction (XRD) patterns of s-CTGS and sintered compounds in each of Series, I, II and III.

3.3 Secondary phase identification via BEI observations

The BEI observations revealed that one or two phases among four secondary phases could coexist with the matrix CTGS phase: $Ca_3Ta_2Ga_4O_{14}$ (CTG), $CaTa_2O_6$ (CT2), $CaSi_2O_5$ (CS2), and $Ca_3Ga_4Si_2O_{14}$ (CGS). The population and coexistence of secondary phases exhibited a clear relationship with the initial bulk compositions.

For quantitative analyses of the populations of secondary phases in the CTGS matrix, 20 BEIs were collected for each sample continuously (Fig. 3.6). The computer software called ImageJ was used to measure the populations of secondary phases for each image. The proportion of secondary phases and its change with initial composition will be discussed in Section 3.5.

Fig. 3.7 (s) presents a BEI of the s-CTGS specimen termed sample (s). A secondary phase, $Ca_3Ta_2Ga_4O_{14}$ (CTG), is evident in this sample, indicating either that CTG may be an equilibrium phase and the s-CTGS composition might not be found in its solid-solution region or that CTG may represent an unreacted non-equilibrium phase. We will discuss this issue in Section 3.5. It should be noted that the presence of this small amount of secondary phase was discernible only through the BEI observations and not by XRD analysis.

Figs. 3.7 (a) and (b) show images of Series I samples, in which the Ta_2O_5 concentrations were constant but the Ga_2O_3-SiO_2 levels were variable. Fig. 3.7 (a) shows that the matrix CTGS phase coexisted with $Ca_3Ta_2Ga_4O_{14}$ (CTG) in the Ga-rich samples. Clear boundaries between the secondary phases and the matrix phase are evident in the BEIs, since the average atomic number of the CTG phase is 39.8 while that of the CTGS matrix is 31.2 (Table 3.2). In contrast, the Ga-poor sample in Fig. 3.7 (b) exhibits $CaTa_2O_6$ (CT2) and $CaSi_2O_5$ (CS2) secondary phases in the CTGS matrix. The average atomic number of the CT2 phase is 56.2 while that of the CS2 phase is 12.6 (Table 3.2), thus the CT2 and CS2 phases are easily distinguished from the CTGS matrix.

Similar observations and analyses were performed with the Series II samples, Figs. 3.7 (c) and (d) show images of Series II samples, in which the SiO_2 level was constant and the Ga_2O_3-Ta_2O_5 concentrations varied. In the Ga-rich sample (c), the matrix phase was CTGS while the secondary phases were CTG and $Ca_3Ga_2Si_4O_{13}$ (CGS). In the Ga-poor sample (d), the secondary phase in the CTGS matrix was CT2. The average atomic number of the CGS phase is 20.4, and thus CGS is distinguishable

from the CTGS matrix and from the secondary phase of CTG.

The Series III samples have the Ga_2O_3 concentration constant while the SiO_2-Ta_2O_5 levels were varied. In Fig. 3.7 (e) and (f), the matrix phase coexisted with CT2 and CTG in the Ta-rich sample (e), while in the Ta-poor sample (f) the secondary phases were CTG and CGS. Again, it should be noted that BEI analysis was a more effective means of evaluating the presence of secondary phases than XRD analysis since it was able to distinguish minute amounts of secondary phases that could not be detected by XRD analysis, as was the case for samples (c), (e) and (f).

Table 3.2 Average atomic number of CTGS and secondary phases.

	CTGS	CTG	CT2	CS2	CGS
Average atomic number	31.2	39.8	56.2	12.6	20.4

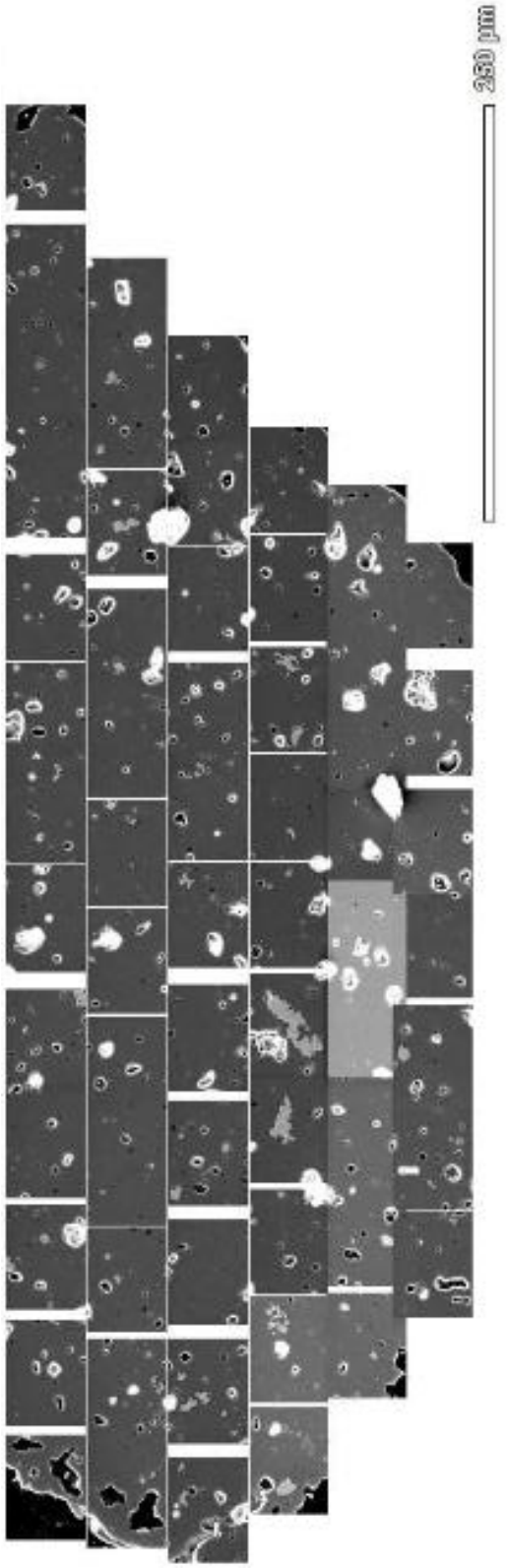

Fig. 3.6 Array of BEI pictures of s-CTGS.

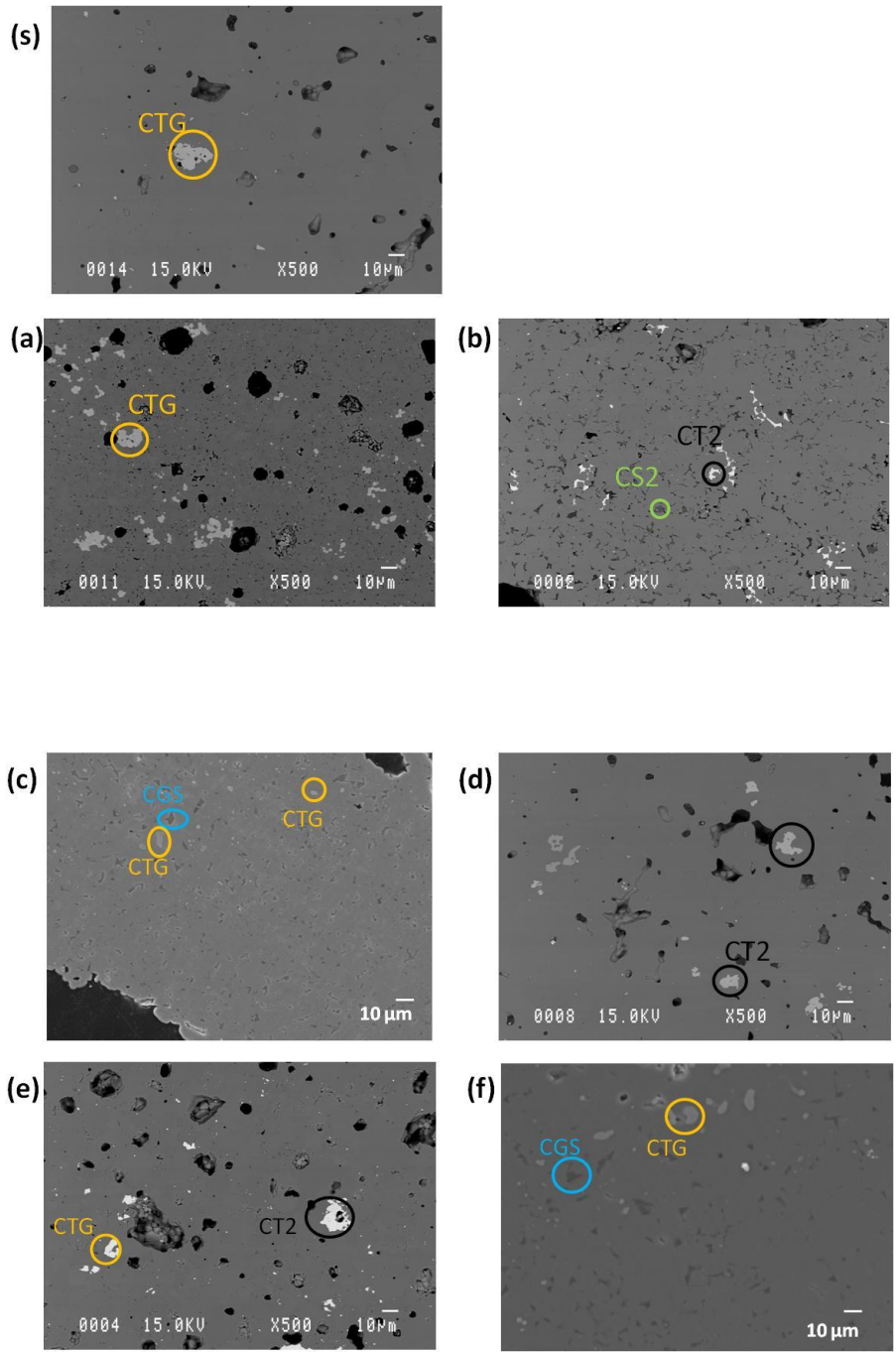

Fig. 3.7 BEIs of sintered compounds with stoichiometric composition: (s) and non-stoichiometric compositions: (a) and (b) from Series I, (c) and (d) from Series II, (e) and (f) from Series III [39].

3.4 Phase diagram of CTGS at elevated temperatures

We applied a lever rule to changes in the proportions of secondary phases coexisting with the CTGS matrix with variations of the initial bulk composition in order to determine the CTGS boundary compositions that define the solid-solution region. During this process, we dealt exclusively with the pseudo-ternary system Ta_2O_5-Ga_2O_3-SiO_2, keeping the CaO concentration constant. The equilibrium tie-line diagram for this system is illustrated schematically in Fig. 3.8 (a). The initial composition that results in an equilibrium assembly of two secondary phases and the CTGS matrix lies in a three-phase triangle (dotted region), while the composition associated with one single secondary phase and CTGS is situated along a two-phase band. This analysis takes the Gibbs phase rule into consideration. The compositions of the two secondary phases and the CTGS matrix were fixed when the initial bulk composition was present in a triangle, since this resulted in zero degrees of freedom. In contrast, the compositions of the single secondary phase and the CTGS were both variable when the initial bulk composition was within the two-phase band, since this scenario allowed one degree of freedom. Therefore, a sample having a composition that generated a two-phase assembly was both preferable and beneficial when a lever rule was applied, in terms of ascertaining the boundary compositions of the CTGS solid-solution region.

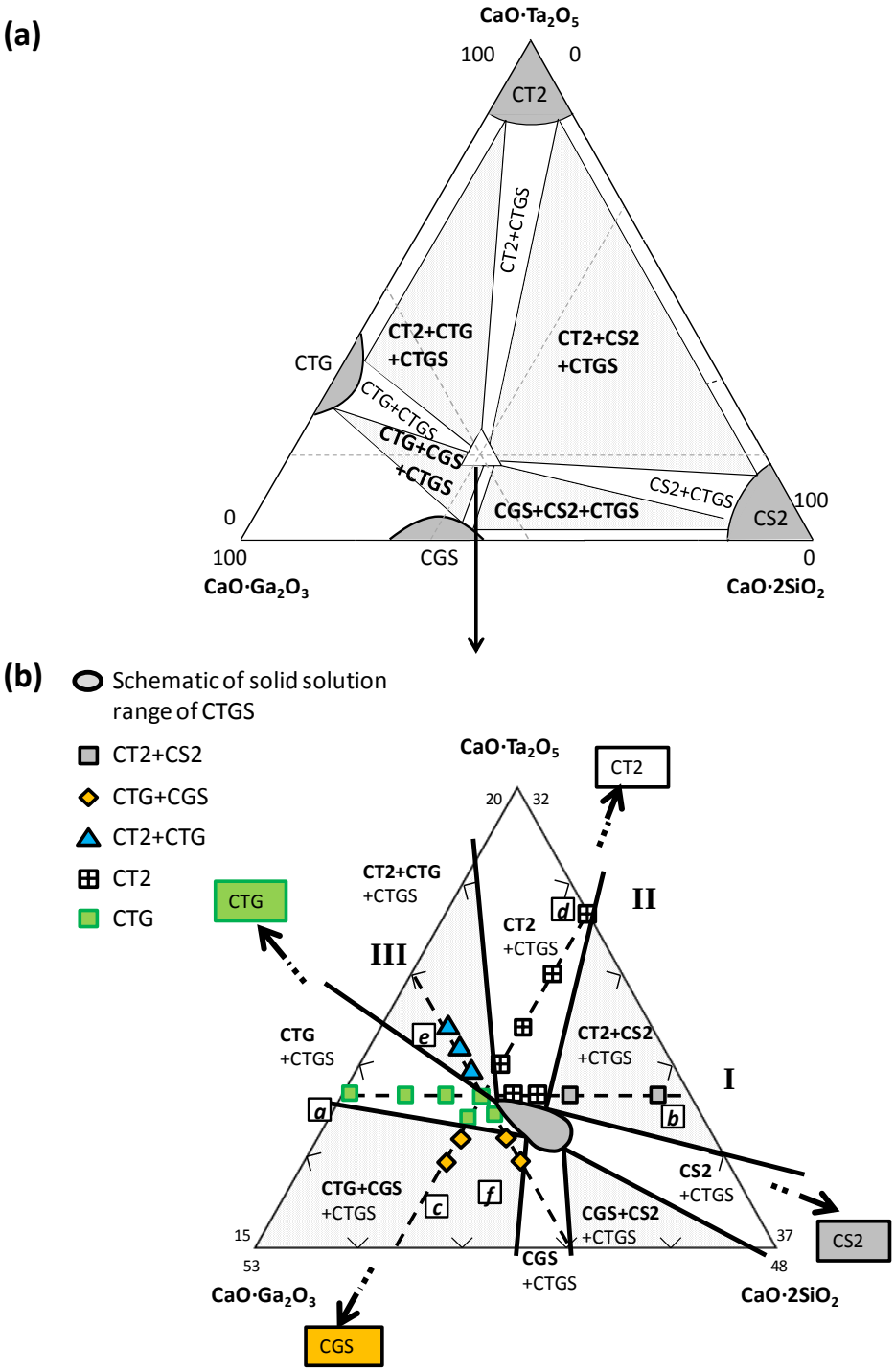

Fig. 3.8 Schematic illustrations of the equilibrium assembly of secondary phases and CTGS in the CaO·Ta_2O_5-CaO·Ga_2O_3-CaO·$2SiO_2$ pseudo-ternary system: (a) equilibrium tie lines. The shaded areas indicate the solid-solution regions for CT2, CTG, CGS and CS2, respectively, (b) equilibrium phase relationships around the presumed CTGS solid-solution region [39].

3.5 Determination of the solid-solution region using the lever rule

The changing proportions of the secondary phases associated with the bulk composition in each series were determined by analyses of BEIs. Many voids with small sizes comparable to those of secondary phases were found. During the lapping and polishing process, we regularly checked the surface of the specimen using an optical microscope. We did not find the removal of secondary phases during these processes. Thus, voids were thought to form during the sintering process. Their population was measured and taken into account for the calculation of the population of the secondary phases. Fig. 3.9 (a) shows the variations of the secondary phase proportions in Series I as the initial bulk composition of Ga_2O_3-SiO_2 is varied. In the region that is Ga-rich relative to the s-CTGS composition (50 mol% Ga_2O_3), the only phase coexisting with CTGS is CTG, and its quantity decreases as the initial bulk concentration of Ga approaches the stoichiometric composition from the Ga-rich side. The minimum CTG concentration is found to be 0.13% at the stoichiometric composition. Thus, the Ga-rich region in Series I is located within the two-phase band composed of CTGS and CTG shown in Fig. 3.8 (b), and the relative proportions of the coexisting CTGS and CTG vary according to the initial bulk composition. A similar analysis was employed for the Ga-poor region in Series I, where some CTGS coexists with CT2 and CS2 phases as shown in Fig. 3.8 (b), and indicated that the Ga-poor region in Series I is possibly present within the three-phase triangle consisting of CTGS, CT2 and CS2. As will be discussed later, however, the composition close to the stoichiometric composition is found in the two-phase band consisting of CTGS and CT2 where CT2 first appears alone. As the composition moves from the two-phase band to the three-phase triangle (Fig. 3.8 (b)), CS2 subsequently joins CT2. According to the phase rule, the compositions of all three phases should be fixed, although their proportions vary in accordance with the initial bulk composition.

The same assessment was carried out for the samples in Series II and III, in which the proportions of the secondary phases coexisting with CTGS changed with the initial bulk compositions variable in the Ga_2O_3-Ta_2O_5 and the Ta_2O_5-SiO_2, respectively. The proportion changes of the secondary phases in Series II are

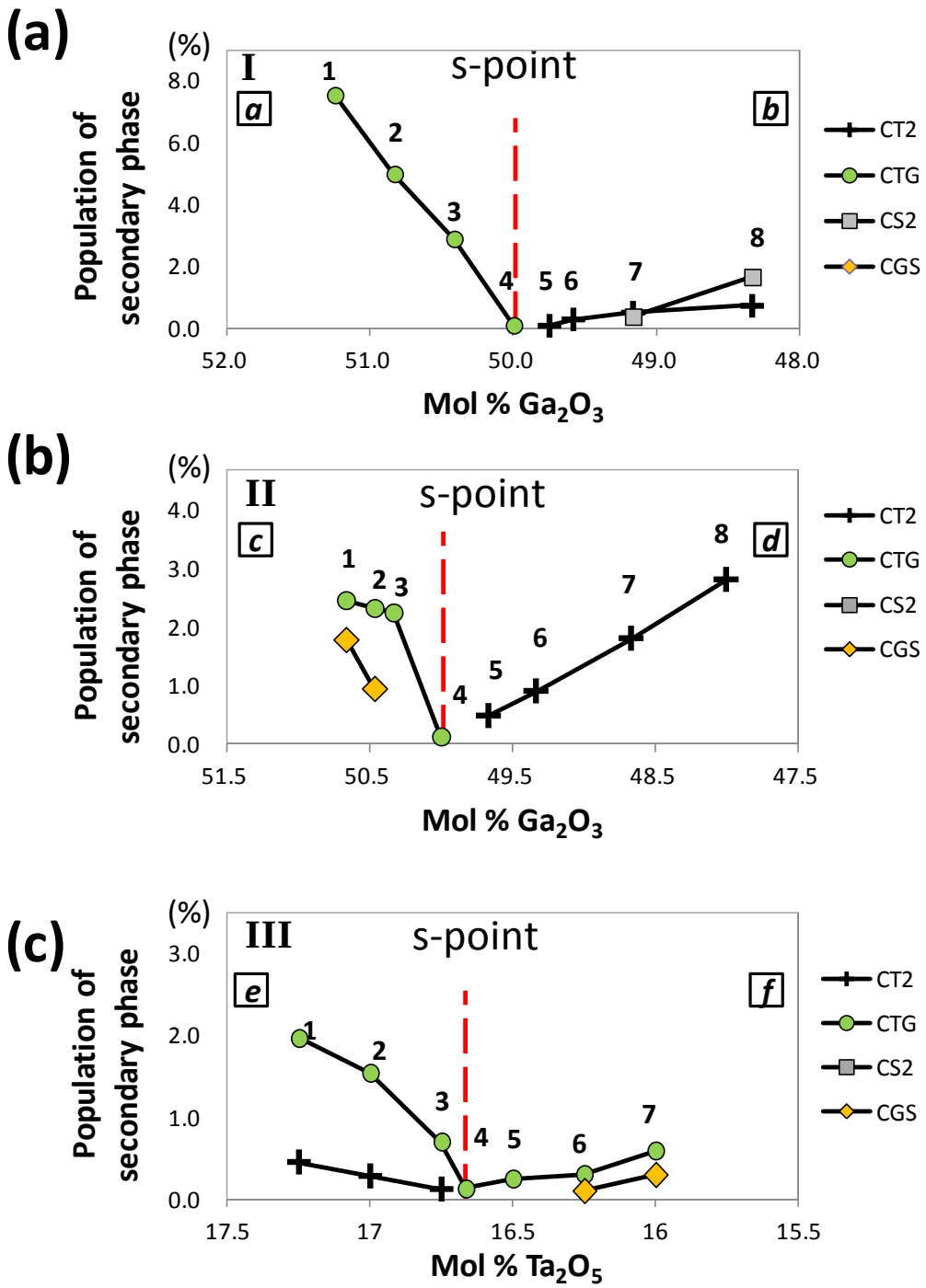

Fig. 3.9 Changes in secondary phase proportions with variations in initial bulk compositions: (a) Series I, (b) Series II, and (c) Series III. The numbers in each graph correspond to those in Fig. 3.10 [39].

summarized in Fig. 3.9 (b). In the region that is Ga-rich relative to the s-CTGS composition (50 mol% Ga_2O_3), CTG first appears near the stoichiometric point, indicating that this bulk composition is included within the two-phase band consisting of CTGS and CTG (Fig. 3.8 (b). This is to be expected based on the above results for Series I. In addition, CGS appears when the initial bulk composition enters the three-phase triangle consisting of CTGS, CTG and CGS (Fig. 3.8 (b)). The proportions of both CTG and CGS are seen to increase as the Ga_2O_3 concentration of the initial bulk composition increases. In the Ga-poor region, CT2 is the only phase coexisting with CTGS and thus this region is found within the two-phase band consisting of CTGS and CT2 (Fig. 3.8 (b)), where the relative proportions are variable depending on the initial bulk composition.

The proportion changes of the secondary phases in the Series III samples are demonstrated in Fig. 3.9 (c). In the region that is Ta-rich relative to the s-CTGS composition (16.7 mol% Ta_2O_5), CT2 and CTG are the secondary phases in equilibrium with CTGS, and the initial compositions are included in the three-phase triangle consisting of CTGS, CT2 and CTG (Fig. 3.8 (b)). Although their proportions vary with the bulk composition, based on the phase rule, all three phases are not expected to exhibit changes in their compositions. In the Ta-poor region, CTG first appears near the stoichiometric point, indicating that its bulk composition is included within the two-phase band consisting of CTGS and CTG (Fig. 3.8 (b)). In addition, CGS appears at the point where the initial bulk composition enters the three-phase triangle consisting of CTGS, CTG and CGS (Fig. 3.8 (b)). This is similar to the case of the Ga-rich composition near the stoichiometric composition in Series II. The proportions of both CTG and CGS are seen to increase as the Ta_2O_5 content of the initial bulk composition decreases. The observed increments in the CTG content are difficult to explain and might simply be artifacts due to the small proportion of CTG in the material.

3.3 mentioned CTG phase was found in sintered material with a s-CTGS composition (Fig. 3.7 (s)). Such CTG was either an unreacted phase or an equilibrium phase. The possibility of an equilibrium phase is due to the following: CTG began to appear at 50 mol% of Ga_2O_3 and its amount increased linearly as the Ga_2O_3 content increased in Series I (Fig. 3.9 (a)) and the same trend was observed in Series II (Fig. 3.9 (b)), which reflects the proportional relationship between the amount of CTG and the excess Ga_2O_3. Thus, the stoichiometric composition of CTGS may not belong to

the solid-solution region of CTGS and might have produced CTG as an excess phase.

Based on the above analysis of the secondary phase proportion changes, we subsequently calculated the boundary compositions of the CTGS solid-solution region by applying a lever rule to the proportions of the secondary phases and the CTGS. This calculation procedure can be illustrated using a Series I specimen as an example. Since the observed CTGS and secondary phase compositions always have the same CaO ratio [Ca/(Ca+Ta+Ga+Si) = 1/3], we need only consider the Ta_2O_5, Ga_2O_3 and SiO_2 components, while holding CaO constant. Applying a lever rule to the volume ratios of secondary phases and the CTGS matrix, the boundary compositions of the CTGS phase were calculated using Eq. 3.2:

$$(1-\sum r_i)\times\begin{pmatrix} t_{ss} \\ g_{ss} \\ s_{ss} \end{pmatrix} = 1\times\begin{pmatrix} t_{int} \\ g_{int} \\ s_{int} \end{pmatrix} - r_{CT2}\times\begin{pmatrix} 100 \\ 0 \\ 0 \end{pmatrix} - r_{CTG}\times\begin{pmatrix} 33.3 \\ 66.7 \\ 0 \end{pmatrix} - r_{CS2}\times\begin{pmatrix} 0 \\ 0 \\ 100 \end{pmatrix} - r_{CGS}\times\begin{pmatrix} 0 \\ 66.7 \\ 33.3 \end{pmatrix} \quad (3.2)$$

where r_i represents the proportion of secondary phase i, and (t_{int}, g_{int}, s_{int}) and (t_{ss}, g_{ss}, s_{ss}) represent the ratios t = Ta/(Ta+Ga+Si), g = Ga/(Ta+Ga+Si) and s = Si/(Ta+Ga+Si) in the initial bulk composition and those in the matrix CTGS solid solution, respectively. For example, the (t_{int}, g_{int}, s_{int}) values are (16.7, 50.0, 33.3) when the initial bulk composition is set equal to the s-CTGS composition. We assume that the compositions of secondary phases are fixed although they show solid solution as shown in Fig. 3.8 (b). We also assume that the there is no difference in density among secondary phases and CTGS. The values of (t, g, s) for $CaTa_2O_6$ (CT2), $Ca_3Ta_2Ga_4O_{14}$ (CTG), $CaSi_2O_5$ (CS2) and $Ca_3Ga_4Si_2O_{13}$ (CGS) are (100, 0, 0), (33.3, 66.7, 0), (0, 0, 100) and (0, 66.7, 33.3), respectively.

The calculated boundary compositions for CTGS in equilibrium with the secondary phases are indicated by solid circles in Fig. 3.10. As illustrated in Fig. 3.8 (b), when the initial bulk composition lies in the two-phase region where CTGS and one secondary phase coexist, one degree of freedom is available for varying the composition of coexisting CTGS. For instance, in Fig. 3.10 (a), compositions 1 through 4 yield CTGS+CTG, and compositions 5 and 6 yield CTGS+CT2. The calculated CTGS compositions corresponding to these initial compositions were varied and form a portion of the boundary of the CTGS solid solution. In contrast, in the case of the three-phase region, compositions 7 and 8 yield CTGS+CT2+CS2 and

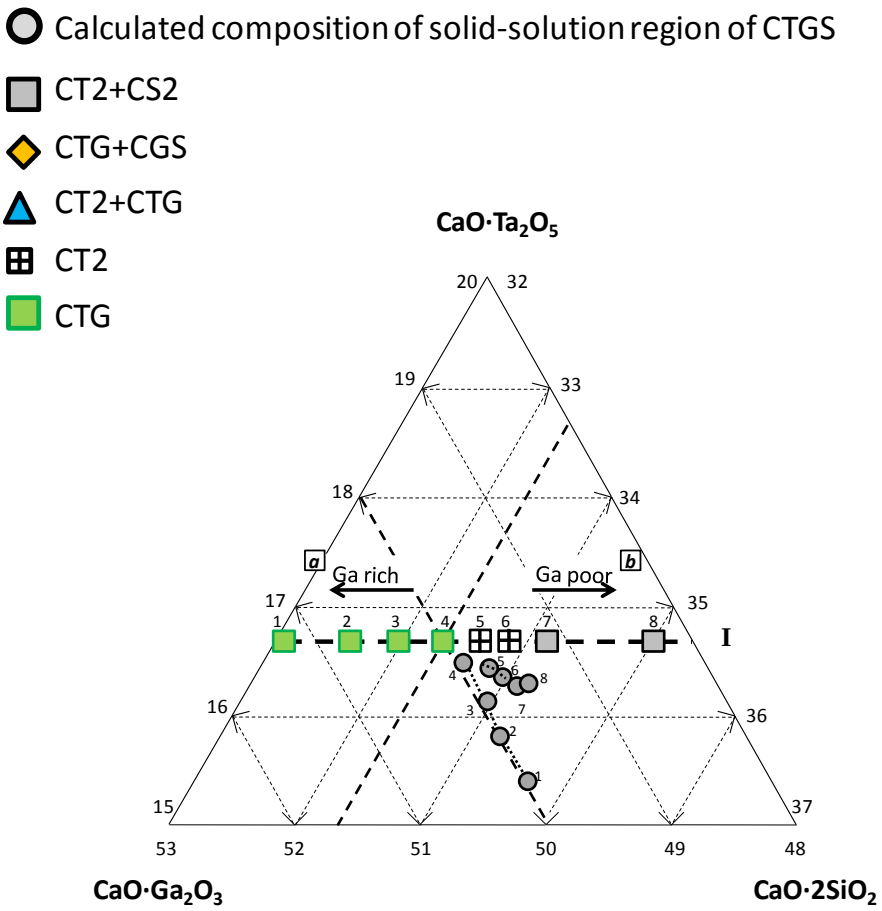

(a)

Fig. 3.10 Boundary compositions of the CTGS solid-solution regiondetermined by a lever rule applied to changes in secondary phase proportions in each series, (a) Series I, (b) Series II, (c) Series III. The numbers in the plots in each series correspond to those in Fig. 3.9. The solid circles in each plot indicate calculated boundary compositions of CTGS solid solution. Solid circles encircled by the dotted line were calculated from the initial composition in the three-phase region, while the other solid circles were calculated from the compositions in the two-phase region in Fig. 3.8 (b) [39].

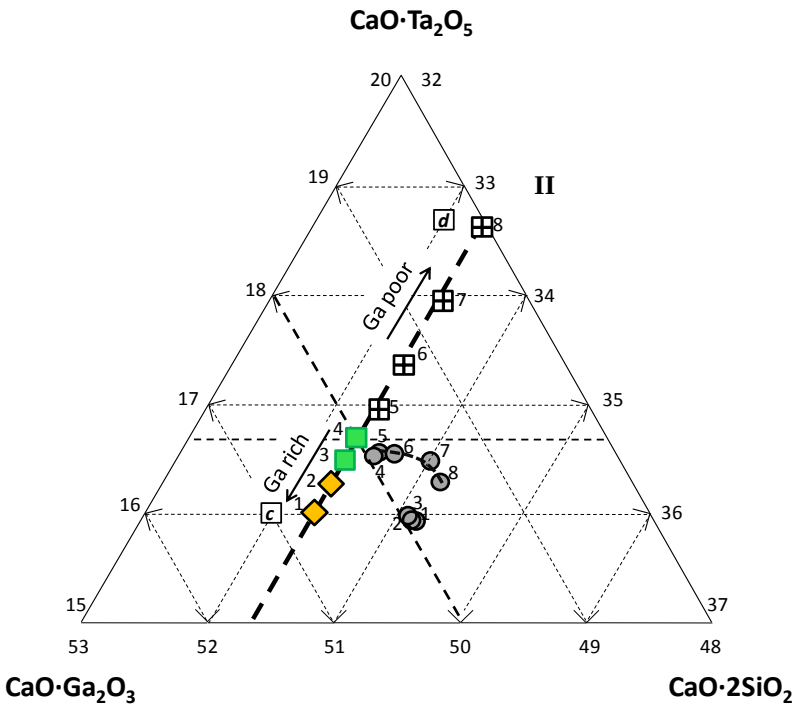
CaO·Ta2O5
20
32
19
33
II
d
8
18
Ga poor
7
34
6
17
5
35
4
5
Ga rich
3
6
7
2
4
8
16
c
1
3
36
15
37
53
52
51
50
49
48
CaO·Ga2O3
CaO·2SiO2

(b)

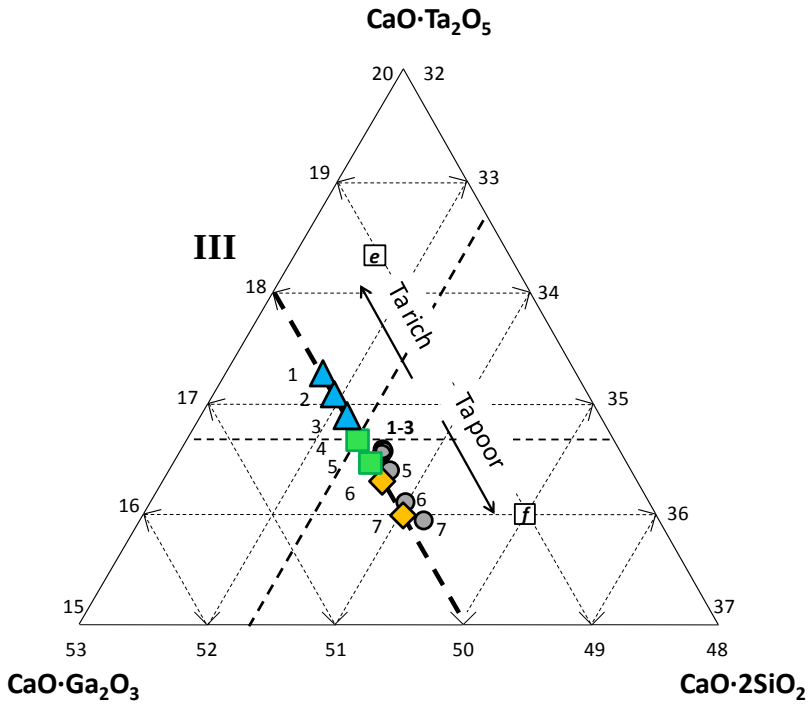
CaO·Ta2O5
20
32
19
33
III
e
18
Ta rich
34
1
17
2
35
3
1-3
Ta poor
4
5
5
6
16
6
f
36
7
7
15
37
53
52
51
50
49
48
CaO·Ga2O3
CaO·2SiO2

(c)

Fig. 3.10

the corresponding compositions of CTGS converge due to the absence of any degrees of freedom; this region is enclosed by the dotted line in the figure. Ideally these values should all converge, although the experimental results do not show complete convergence. The calculated boundary compositions for CTGS in equilibrium with secondary phases in Series II and III were also calculated and are presented in Figs. 3.10(b) and (c), respectively. Using the results shown in Figs. 3.10(a) to (c), the CTGS solid-solution region was eventually determined, and is represented by the gray shaded region in Fig. 3.11. The solid boundary line was experimentally obtained whereas the dotted line is the estimated one. The CTGS solid-solution region was determined to be CaO-Ta_2O_5: 15.9-16.6 mol%; CaO-Ga_2O_3: 49.6-49.9 mol%; and CaO-$2SiO_2$: 33.4-34.3 mol%. The solid-solution region for CTGS is elongated parallel to the Ta_2O_5-SiO_2 line occupying Ta_2O_5-poor, slightly Ga_2O_3-poor and slightly SiO_2-rich regions.

The results of the solid-solution region determination support the crystal-site structure of the V_B model: vacancies are required at the B site to compensate the charge imbalance at the C site. CTGS has a narrow solid-solution region compared with langasite-type crystals with three elements, which suggests that CTGS is a more promising material for high-temperature pressure sensors. The procedure used in this study is novel and is applicable to assess the solid-solution regions for other complex oxide materials.

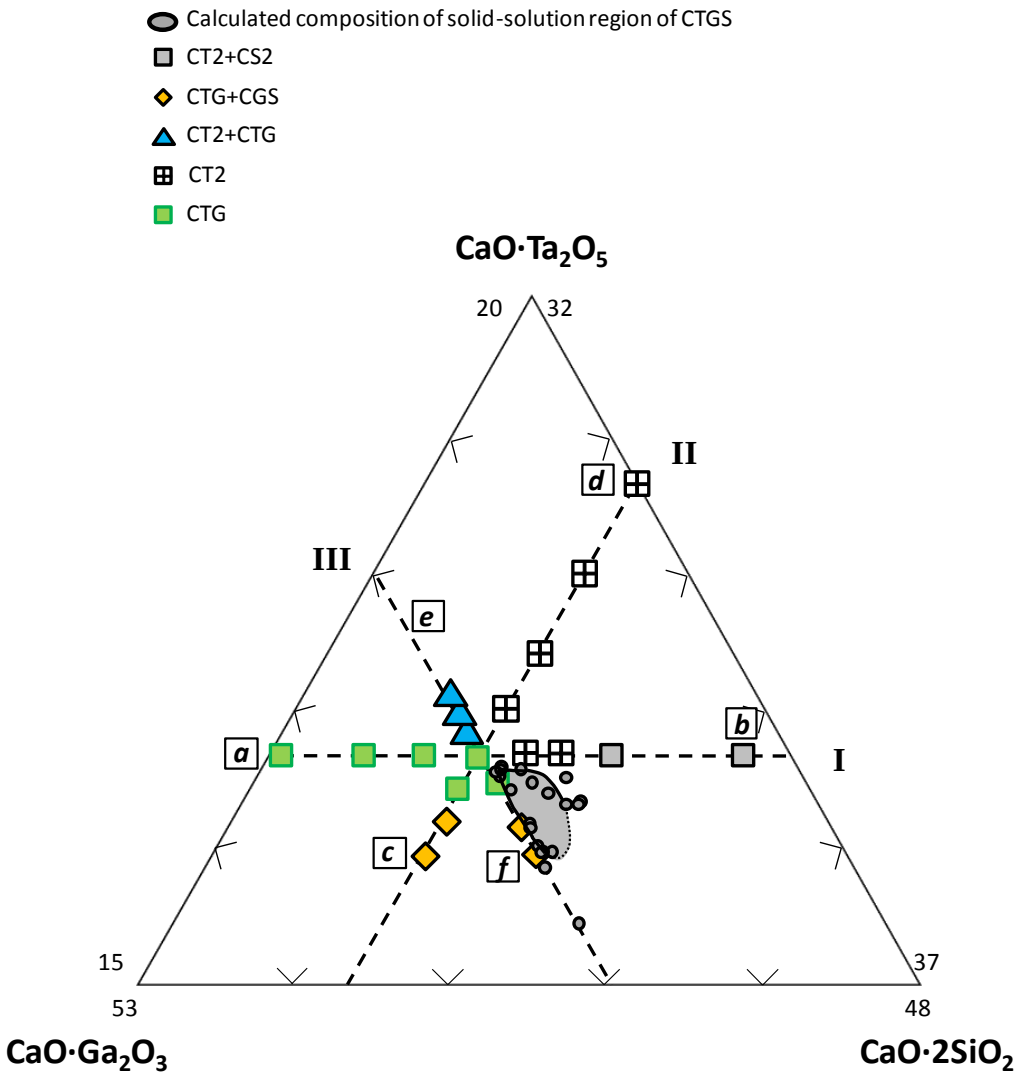

Fig. 3.11 Solid-solution region for CTGS. The solid boundary line was experimentally obtained, whereas the dotted line was estimated [39].

3.6 Summary

We have applied a lever rule to data regarding the secondary phases and the CTGS matrix associated with various bulk compositions around the s-CTGS composition. Secondary phases were found to form in the CTGS matrices of sintered materials and their compositions and proportions were investigated by EPMA and BEIs. The data indicate that the CTGS solid-solution region is elongated parallel to the Ta_2O_5-SiO_2 line, and occupies a Ta_2O_5-poor, slightly Ga_2O_3-poor and slightly SiO_2-rich region. The procedure applied in this study was novel and should be applicable to the assessment of the solid-solution regions for other complex materials.

1. Conventional XRD analysis was insufficient to determine the solid-solution region for CTGS because the intensities of the secondary-phase reflection peaks were not sufficiently strong to allow quantitative analysis.
2. The variation of proportions of the secondary phases associated with the bulk composition in each series was determined via BEI observations. The boundary compositions of the CTGS solid-solution region were determined by applying a lever rule to the proportions of the secondary phases and CTGS in combination with the composition of the secondary phase.
3. Solid-solution region of CTGS was determined to be, CaO-Ta_2O_5: 15.9-16.6 mol%; CaO-Ga_2O_3: 49.6-49.9 mol%; and CaO-$2SiO_2$: 33.4-34.3 mol%. The solid-solution region of CTGS is elongated parallel to the Ta_2O_5–SiO_2 line and occupies a Ta_2O_5-poor, slightly Ga_2O_3-poor, and slightly SiO_2-rich region, which supports the V_B model of crystal-site structure: vacancies are required in the B site to compensate the charge imbalance in the C site.

Chapter 4 Congruency, crystal growth, and liquid immiscibility of CTGS

This chapter discusses the crystal growth of CTGS. The congruency of a crystal is crucial for ensuring the growth of homogeneous crystals that have reliable physical properties for device applications. Langasite-type crystals with three elements, such as langasite (LGS, $La_3Ga_5SiO_{14}$) and langatate (LTG, $La_3Ta_{0.5}Ga_{5.5}O_{14}$), have been shown to be incongruent [34,40], which causes fatal polycrystallization defects during growth. Therefore, for the large-scale growth of crystals intended for use as pressure sensors at high temperatures, a congruent langasite-type crystal with four elements is desired. Differential thermal analysis (DTA) was thus employed to examine the congruency of CTGS.

Liquid–liquid phase separation, referred to as liquid immiscibility, has been studied as an important differentiation mechanism in silicate melts [41-43]. The occurrence of liquid immiscibility is harmful to crystal growth because this phenomenon results in the formation of a secondary phase in the host crystal. Liquid immiscibility has been reported in langasite-type crystals with three elements [44]. However, the existence of liquid immiscibility in langasite-type crystals with four elements is yet unknown.

4.1 Experimental

4.1.1 DTA measurement of stoichiometric CTGS

To study the congruency of CTGS, DTA measurements were obtained using a Linseis DTA/DSC PT1600 under an air atmosphere with heating and cooling rates of 20 ℃/min. Pt crucibles were used for the sample and the reference. Stoichiometric CTGS (s-CTGS) (50 mg) was placed in the sample crucible, while the reference crucible remained empty. For temperature calibration, the melting point of Au (1064.4 ℃) was used and confirmed before and after the measurement of CTGS. Thus, the accuracy of the DTA data for CTGS was assured.

4.1.2 Crystal growth of CTGS using the micro-pulling-down technique

A CTGS bulk crystal was grown using the micro-pulling-down technique (μ-PD technique), schematically shown in Fig. 4.1. A pipe-shaped capillary with a length of 1 mm and a diameter of 2 mm was attached to the bottom of the container portion of the crucible. The container portion of the crucible comprised Pt–Rh (10% Rh), while the capillary was pure Pt. Electric power (5 V, ~10 A) was applied directly to the Pt–Rh crucible for self-heating. The temperature of the melt was controlled by varying the current supplied to the crucible. The after-heater in the furnace was placed 2 cm below the capillary and was set at 800 ℃. Assuming that the temperature of the liquid–solid interface was approximately 1430 ℃ (see Section 4.2), the temperature gradient at the interface was in the range from 500–700 ℃/cm. A langatate crystal with a *c*-axis orientation was used as a seed to grow the CTGS crystal because langatate has the same crystal structure as CTGS, which results in only a slight mismatch of the crystal lattice; thus, a low degree of distortion and a high degree of coherency was achieved in the lattice of the obtained CTGS crystal. In addition, the melting point of langatate is approximately 1450 ℃, which is close to that of CTGS (1430 ℃). The langatate seed crystal was moved upward until it contacted the CTGS melt at the tip of the capillary. CTGS crystal was then grown by pulling down the seed at the rate of 2 mm per hour. The interface of the melt and the crystal was

observed during crystal growth (Fig. 4.2). The growth conditions are listed in Table 4.1.

Table 4.1 CTGS crystal growth condition

Crystal growth technique	μ-PD technique
Atmosphere	Air
Crucible	Pt + 10%Rh
Capillary	Length: 1 mm. Diameter: 2 mm
Applied power	5 V, ~10 A
Seed crystal	Langatate with *c*-axis orientation
Growth rate/pulling-down velocity	2 mm/h
After-heater	800 ℃

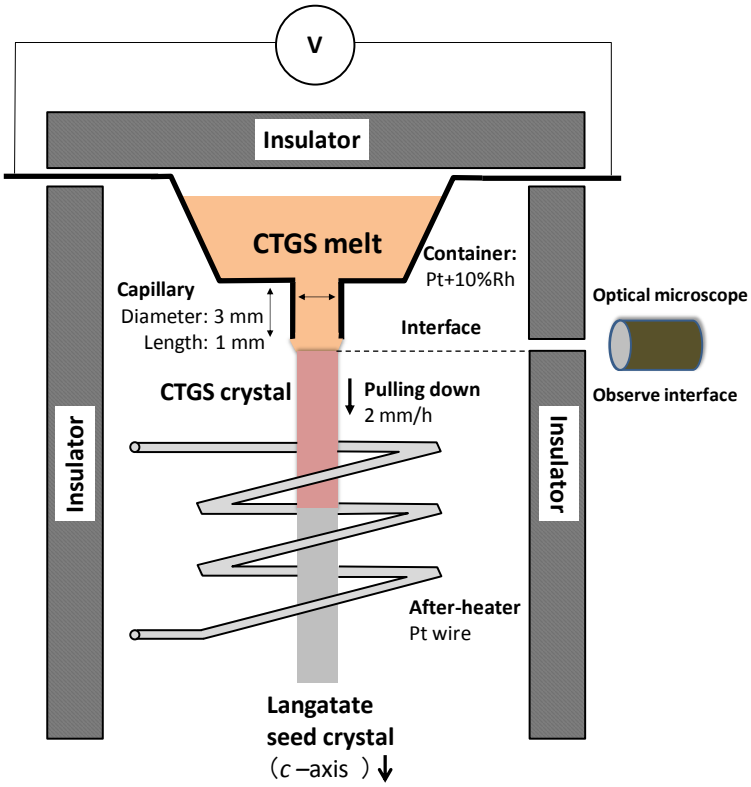

Fig. 4.1 Schematic of the μ-PD furnace used to grow CTGS crystals. During the crystal growth, the solid–liquid interface was observed using an optical microscope.

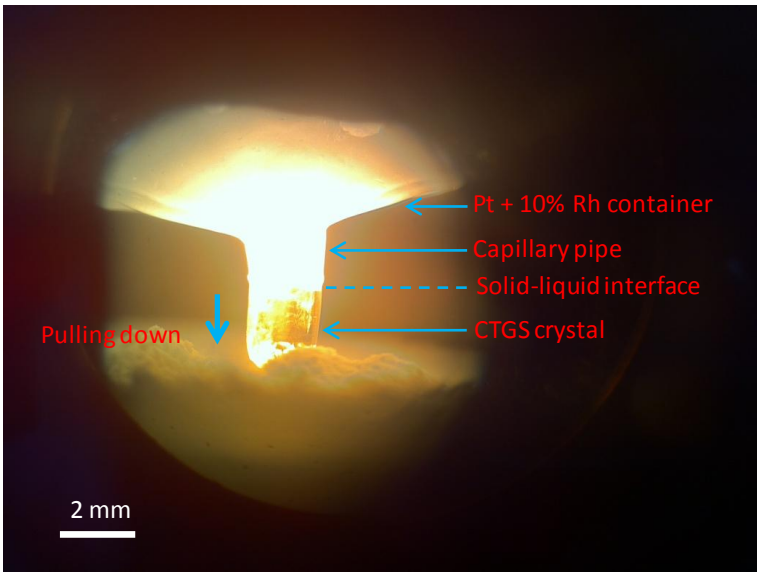

Fig. 4.2 Optical microscopy image of the solid–liquid interface during growth of CTGS.

4.2 Results

4.2.1 Congruency of CTGS

Two cycles of DTA plots for the melting and solidification of s-CTGS are shown in Fig. 4.3. Fig. 4.3 (a) presents the curves obtained during heating of the sample to 1650 ℃, while Fig. 4.3 (b) shows the curves obtained during heating to 1490 ℃.

In Fig. 4.3 (a), endothermic peaks near 1430 ℃ in both the cycles represent the CTGS melting. Notably, the composition of the sintered CTGS sample used for the DTA measurement is that of sample(s), as listed in Table 3.1. Sample(s) contained a 0.13% CTG secondary phase; however, for this CTG phase, no endothermic peak appeared during the heating process because of very low content of CTG phase. During the cooling process for both cycles, the minor peaks near 1285 ℃ indicate the solidification of CTGS from the melt. These peaks have weak intensities because much of the melt remains in a glassy state during cooling. The exothermic peak observed during heating in the 2^{nd} cycle indicates the transition of CTGS from the glassy to the crystalline state. Notably, both cycles exhibit a pair of endothermic and exothermic peaks, demonstrating that CTGS is congruent.

When the sample was heated to 1490 ℃ (Fig. 4.3 (b)), melting peaks near 1430 ℃ were observed in both cycles, as were observed when the sample was heated to 1650 ℃. However, during the cooling process, an exothermic peak appeared at 1280 ℃ followed by a smaller exothermic peak at 1160 ℃. This smaller peak may represent the crystallization of the secondary phase, which was not detected when the sample was heated to 1650 ℃. Therefore, the difference in the maximum heating temperature led to this difference, and its cause is discussed in Section 4.3.

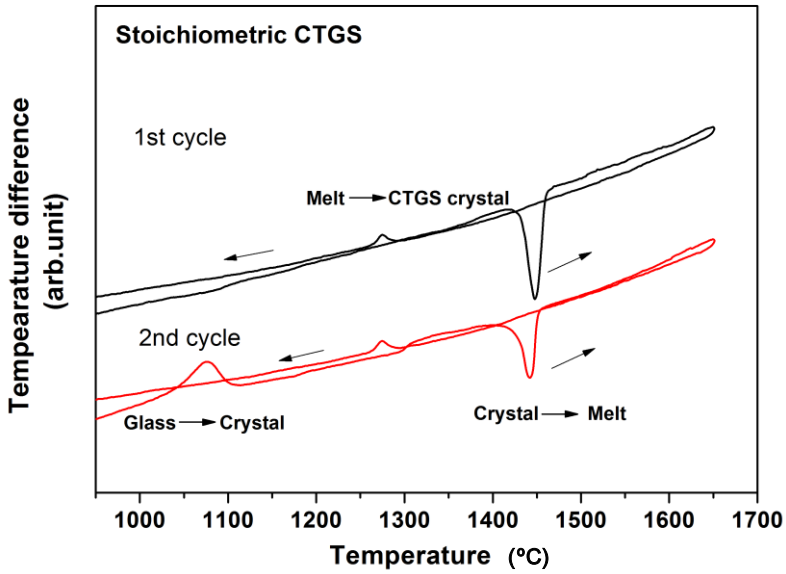

(a)

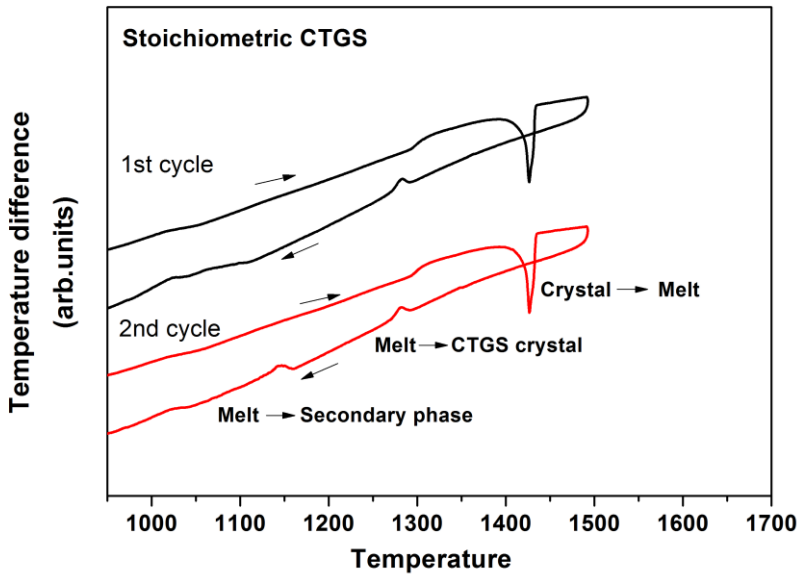

(b)

Fig. 4.3 Two cycles of DTA plots for the melting and solidification of sintered CTGS with a stoichiometric composition: (a) heated to 1650 ℃ and (b) heated to 1490 ℃.

4.2.2 Crystal growth of CTGS and secondary phase observation via BEI analysis

A colorless and transparent CTGS single crystal with a mass of 120 mg, a length of 7 mm, and a diameter of 2 mm was obtained via μ-PD growth (Fig. 4.4). To evaluate the degree of homogeneity of the crystal and to determine whether any secondary phases were present in CTGS crystal, a cross section of the obtained crystal was subjected to BEI observation. The specimen was cut from the top portion of the obtained CTGS crystal and mirror polished.

BEI analysis revealed secondary phases as white spheres (Fig. 4.5). The compositions of the matrix and secondary phases were determined via electron-probe microanalysis (EPMA). The matrix phase of CTGS investigated in Chapter 3 was rich in Si and poor in Ga and Ta. On the contrary, the secondary phase was identified as a Ca–Ta–Ga oxide (CTG). The compositions of the matrix CTGS and secondary CTG phases are presented in Table 4.2. Notably, CTG appeared in the early stage of CTGS crystallization.

Many groups have reported that CTGS crystals grown using the Czochralski (Cz) technique do not appear to have secondary phases [26-29]. However, these groups did not confirm the absence of secondary phases that might be hiding in the melt that remained separate from the growing crystal. However, with the μ-PD method, all the melt is consumed, and therefore, secondary phases cannot stay hidden. In addition, Yokota et al. [30] observed a secondary phase in the peripheral portion of a CTGS crystal grown from a stoichiometric melt using the μ-PD technique, which is similar to the result obtained in the present study.

Table 4.2 Compositions of the host CTGS and the secondary CTG phases in CTGS crystal grown using the μ-PD technique. The values indicate the atomic ratios.

	Matrix phase: CTGS	Secondary phase: CTG
Ca	2.94	3.53
Ta	0.99	2.12
Ga	2.53	3.19
Si	2.54	0.16
O	15.18	15.44

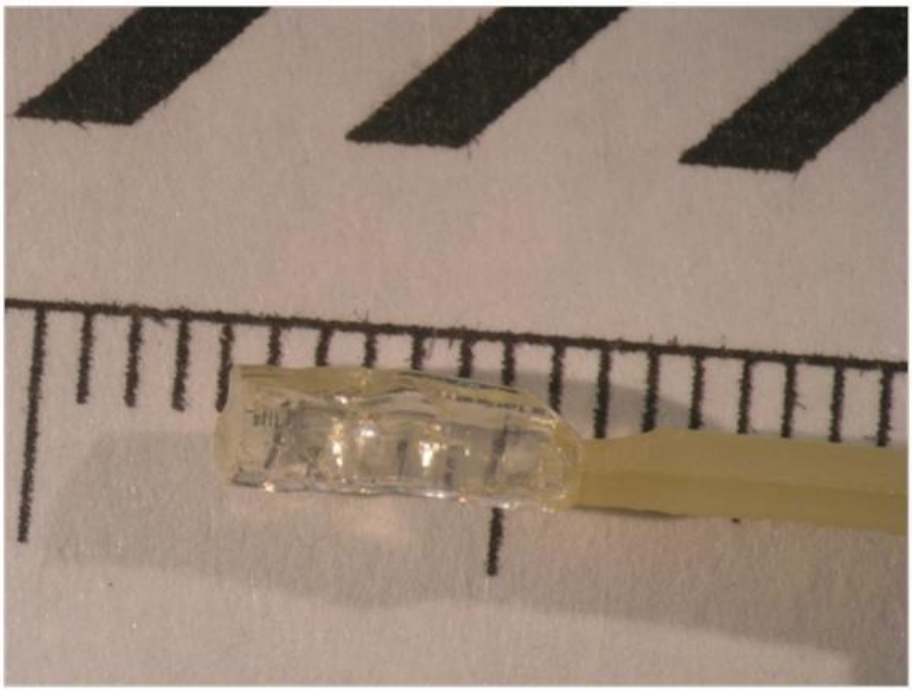

Fig. 4.4 CTGS bulk crystal grown using the μ-PD method.

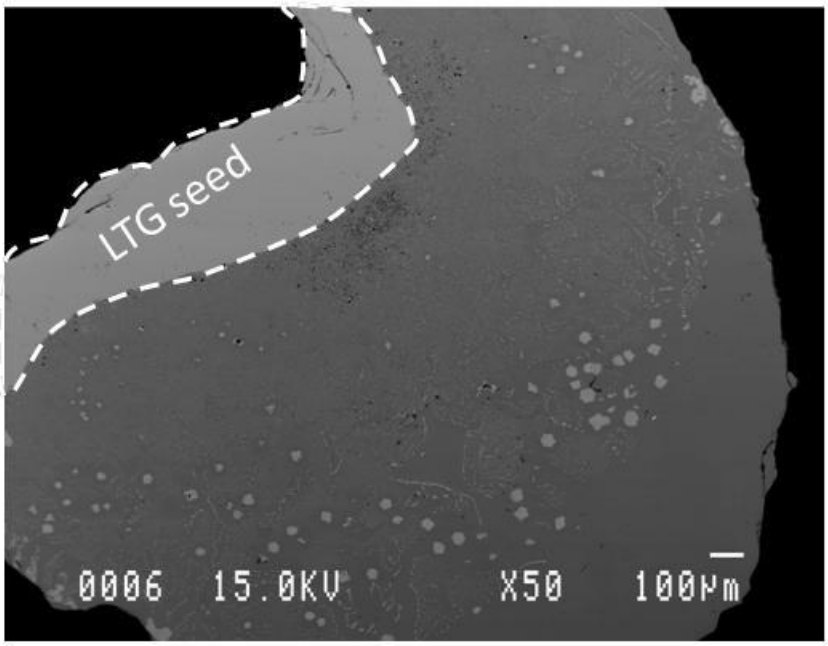

Fig. 4.5 BEI of a cross section of CTGS crystal.

4.3 Liquid immiscibility in CTGS melts

Preventing the formation of secondary phases is a critical issue for obtaining high-quality, large single crystals. Clarifying the formation mechanism of secondary phases should enable the identification of methods for suppressing their formation. Thus, the formation mechanism of the secondary phase during CTGS growth was investigated. Three possible mechanisms were considered: incongruency, eutectic reaction, and liquid immisicbility.

Incongruency of a material yields a primary phase different from the host phase during the early stage of the cooling process. However, CTGS is a congruently melting material (see Fig. 4.3 (a) in Section 4.2.1).

The eutectic reaction yields a secondary phase when the melt reaches the eutectic point. As described above in Chapter 3, the stoichiometric composition of CTGS was found to be outside the solid-solution region. The schematic phase diagram for CTGS–CTG binary system is shown in Fig. 4.6. During CTGS crystallization, the composition of the melt travels along the liquidus line, and the secondary CTG phase appears when the composition of the melt reaches the eutectic point (e). However, such a secondary phase induced by the eutectic reaction only forms during the late stage of crystal growth. In the present study, CTG phase was observed during the very beginning stage of crystal growth (Fig. 4.5), which indicates that it was not formed because of the eutectic reaction.

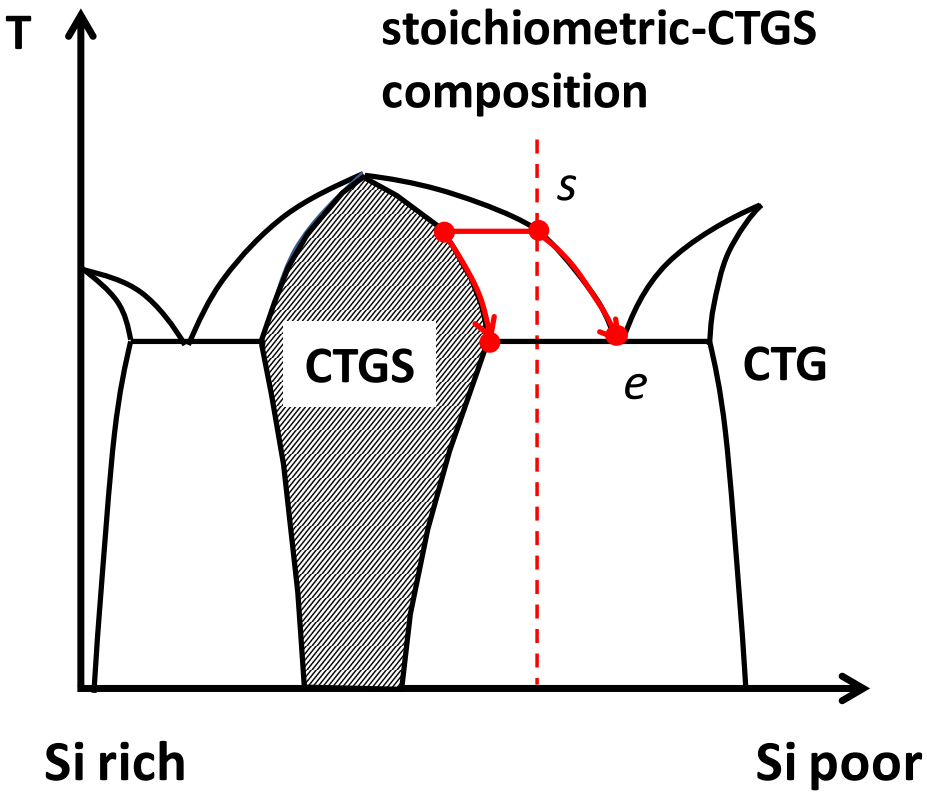

Fig. 4.6 Schematic phase diagram for the pseudo-binary CTGS–CTG system assuming a eutectic reaction. The melt changes its composition along the liquidus line from points *s* to *e* during crystallization of CTGS. CTG joins where the melt reaches the eutectic point *e*.

The extra exothermic peaks near 1280 ℃ in the DTA curves obtained when CTGS sample was heated to 1490 ℃, which indicate the appearance of CTG secondary phase in CTGS bulk crystal, can be explained by liquid immiscibility. When the melt with a s-CTGS composition was cooled down from 1490 ℃, liquid–liquid phase separation possibly occurred prior to initiation of the solidification process, leading to differentiation into Si-poor and Si-rich melts (Fig. 4.7). CTGS subsequently crystallized from the Si-rich melt, while CTG secondary phase precipitated from the Si-poor melt. However, the melt cooled from 1650 ℃ did not experience such a phase seperation but directly reached CTGS liquidus line.

Therefore, phase separation during CTGS growth presumably occurs under conditions in which the temperature at the liquid–solid interface is lower than 1490 ℃. Fig. 4.8 presents a magnified version of the BEI image of CTGS melt/langatate seed crystal contact area (Fig. 4.5). The white spherical shapes with diameters of several microns are CTG secondary phase.

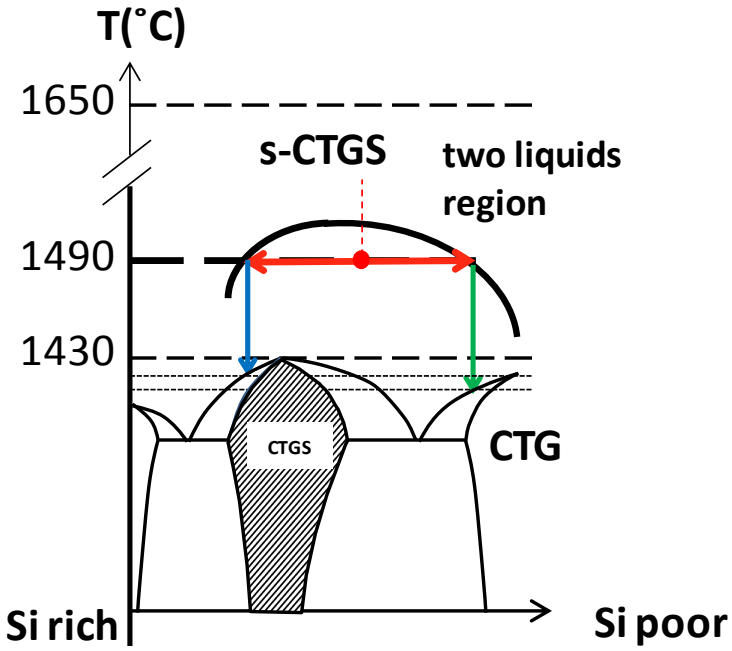

(a)

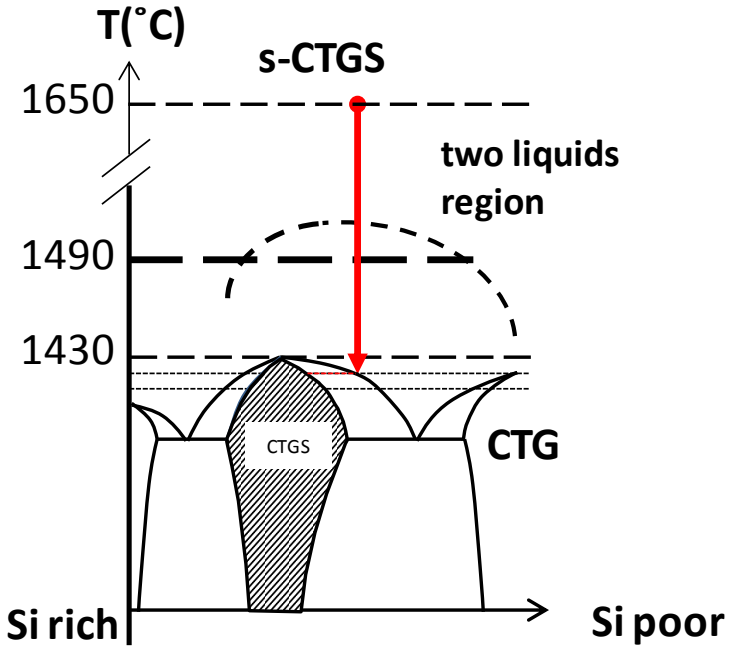

(b)

Fig. 4.7 Schematic phase diagram of CTGS–CTG system showing the liquid immiscibility gap in CTGS melt. (a) Cooled down from 1490 ℃ and (b) cooled down from 1650 ℃.

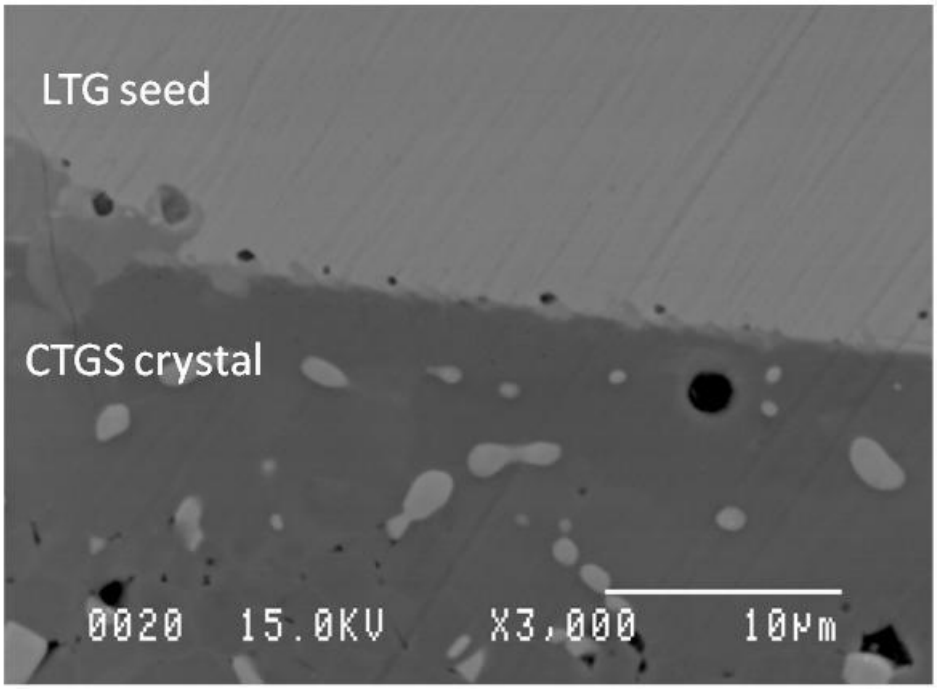

Fig. 4.8 BEI of CTGS crystal near the seed. The white spheres are CTG. Note that they appeared during the early stage of CTGS growth.

4.4 Summary

The congruency and liquid immiscibility of CTGS were investigated, and the formation mechanism of CTG secondary phase that is present in CTGS crystal was clarified.

1. CTGS was shown to be a congruently melting material, with only a pair of melting and solidification peaks observed in the DTA curves. Considering that langasite-type crystals with three elements are known to be incongruently melting materials, CTGS, which is a langasite-type crystal with four elements, is advantageous for crystal growth.
2. Colorless and transparent CTGS crystal was grown using the μ-PD technique. It contained a secondary phase that was determined to be CTG. Using EPMA, the composition of the host CTGS phase was determined to be rich in Si and poor in Ga and Ta and to fall in the solid-solution region.
3. Liquid–liquid phase separation occurred in the s-CTGS melt near 1490 ℃, and Si-rich and Si-poor melts were formed. The host CTGS crystal solidified from the Si-rich melt that belonged to the solid-solution region, whereas CTG secondary phase precipitated from the Si-poor melt.

Chapter 5 Conclusion

CTGS is a promising candidate for pressure sensors used at high temperatures because it is a piezoelectric material with high electrical resistivity that is dominated by the locations and population of the metal vacancies. Thus, the locations of metal vacancies in CTGS crystal-site structure were investigated. Then crystal-site structures and solid-solution region for crystalline CTGS have been determined. The thesis comprises five chapters as follows.

In Chapter 1, the objective of the current research, which was to determine the locations of metal vacancies in four-element langasite-type crystals such as CTGS, was explained. The relation between the resistivity of langasite-type crystals and the locations of metal vacancies in the crystal site structure was also introduced.

In Chapter 2, possible crystal-site structures in CTGS were proposed, and the possible sites for metal vacancies in each were noted. Methods for reducing the number of possible crystal-site structure were then outlined. First, the possible crystal sites for constituent Ca, Ta, Ga, and Si atoms were evaluated using the Hume–Rothery rules, and eight crystal-site structures were proposed. The number of possible crystal-site structures was then further reduced by considering the degrees of freedom in the crystal sites. Finally, three crystal-site structures were concluded as viable for CTGS.

In Chapter 3, to determine the solid-solution region for CTGS, a lever rule was applied to the secondary phase and matrix CTGS populations with the compositions of the secondary phases combined. The compositions of the secondary phases were determined using EPMA, while the populations of the secondary phases were examined using BEI analysis. One or two types of the secondary phases were found to coexist with the matrix CTGS phase. These secondary phases included $Ca_3Ta_2Ga_4O_{14}$ (CTG), $CaTa_2O_6$ (CT2), $CaSi_2O_5$ (CS2), and $Ca_3Ga_4Si_2O_{14}$ (CGS). The phase relation at 1320 ℃ between CTGS and the secondary phases was investigated by applying the Gibbs phase rule to the phase assembly of each secondary phase with the matrix CTGS phase. The determined solid-solution region was found to be located in a region with poor Ta, slightly poor Ga, and slightly rich Si compositions on the Ca-1/3 plane. This result indicated that CTGS has a crystal-site structure with a vacancy present at the B site.

In Chapter 4, CTGS was confirmed to be a congruently melting material using

DTA measurement, with only a pair of peaks for melting and solidification appearing in the DTA curves. In addition, the mechanism of secondary phase formation was clarified. Liquid immiscibility may be present in CTGS melts. When identical samples were heated to different maximum temperatures, the DTA reults revealed that a liquid–liquid phase separation occurred at approximately 1490 ℃, resulting in the formation of different Si-poor and Si-rich melts. Notably, this liquid immiscibility was observed during the crystal growth of CTGS using the μ-PD technique. Colorless and transparent CTGS crystals were successfully grown with CTG secondary phases that appeared at the very beginning of the crystal growth process. The host CTGS phase crystallized from the Si-rich melt, while CTG secondary phase precipitated from the Si-poor melt.

The results of this study confirm that CTGS is a promising material for use in high-temperature pressure sensors because it is a congruently melting material that has a limited solid-solution region. In addition, the procedures used in this study for assessing the crystal-site structure and solid-solution region are novel and applicable to other complex oxide materials.

Appendices

A.1 Application of the lever rule for determining the mass fractions of the phases present in a binary system

For a certain composition in a two-phase field of an A-B binary system, the mass fractions of the two stable phases are determined by applying the lever rule. In Fig. A.1, *a* and *c* respectively indicate the compositions of a liquid and solid coexisting at temperature T, where *b* represents the bulk composition. Application of the *lever rule* determines the mass fraction of the liquid (M_L) and solid (M_S) phases. Eq. A.1 represents the lever rule:

$$M_S : M_L = (b - a) : (c - b) \tag{A.1}$$

If *b*, M_S /$M_{L,}$ and *a* (or *c*) are given, *c* (or *a*) can be obtained, while M_S /M_L is obtained for given values for *b*, *a*, and *c*. Thus, the lever rule can be used to determine the chemical compositions of phases or the mass fractions of coexisting phases.

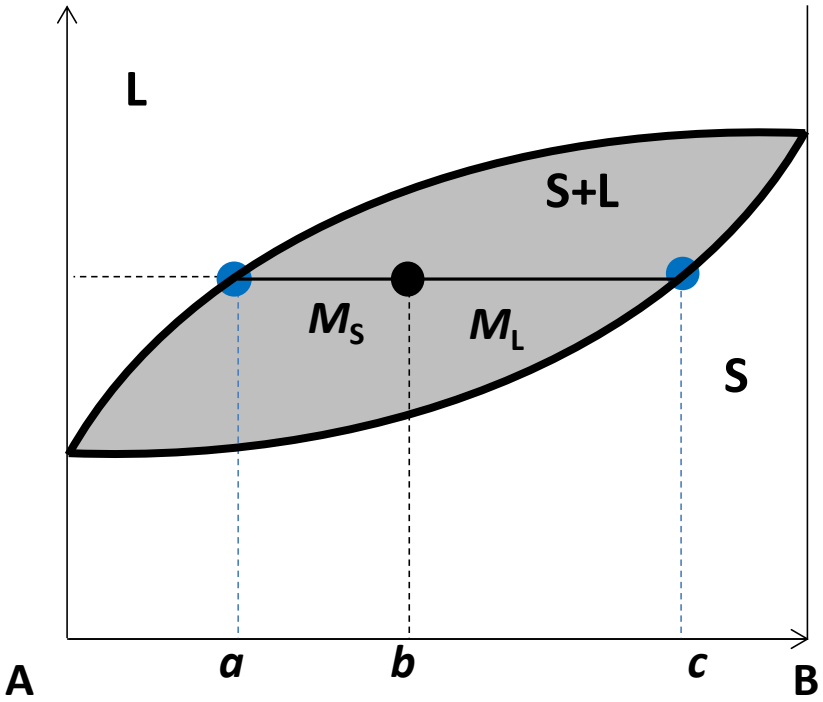

Fig. A.1 Binary (A-B) phase diagram. L: liquid, S: Solid, *a*: composition of the liquid, *b*: initial bulk composition, *c*: composition of the solid, M_S: mass fraction of the solid, M_L: mass fraction of the liquid.

A.2 Application of the lever rule for determining the boundary composition of the solid-solution region in a binary system

In Chapter 3, the lever rule was used to determine the boundary composition of the solid-solution region for CTGS in a CaO–Ta_2O_5–CaO–Ga_2O_3–CaO–SiO_2 pseudo-ternary system (Fig. 3.11). Here, we show the use of the lever rule for determining the boundary composition of the solid-solution region using an AB_2–B binary system as an example. The boundary compositions of the solid-solution regions for the AB_2 phase are determined by providing the initial bulk composition, the mass fraction of the AB_2 or B phase, and the compositions of the B phase that is in equilibrium with the AB_2 phase.

Fig A.2 illustrates the phase diagram of the AB_2–B binary system. The AB_2–B system is described as a B_2A–B_2B system, and thus, the equilibrium compositions of the AB_2 and B phases are represented by $B_2A_{1-m}B_m$ and $B_2A_{1-s}B_s$, respectively. The parameters m and s represent the matrix and secondary phases, respectively. Likewise, the initial bulk composition is represented by $B_2A_{1-i}B_i$, where i stands for "initial." The order of these parameters is $0 \leq m < i < s \leq 1$. The mass fractions of the AB_2 and B phases are $(1 - r)$ and r, respectively. The initial bulk composition, $B_2A_{1-i}B_i$, is given by Eq. A.2:

$$r\ B_2A_{1-s}B_s + (1-r)\ B_2A_{1-m}B_m = B_2A_{1-i}B_i\,. \tag{A.2}$$

Because all three compositions are represented by $B_2A_{1-j}B_j$ ($j = m, i, s$), only the variation of $A_{1-j}B_j$ is considered. Thus, Eq. A.2 is differentiated into the mass conservation equations Eq. A.3a and A.3b for elements A and B, respectively:

$$r\,(1-s) + (1-r)\,(1-m) = 1-i\,, \tag{A.3a}$$

and

$$r\,s + (1-r)\,m = i\,. \qquad \text{(A.3b)}$$

Notably, Eqs. A.3a and A.3b are equivalent.

In Chapter 3, to obtain the boundary composition of CTGS solid-solution region, *r* was experimentally determined, *i* indicated the initial bulk composition that was experimentally established, and *s* indicated the composition of the secondary phase, which was assumed to be 1 for the simple stoichiometric composition. Thus, the boundary composition of the AB_2 solid solution, *m*, was obtained using Eq. A.4, which was deduced from either Eq. A.3a or Eq. A.3b:

$$m = \frac{i - r\,s}{1 - r}\,. \qquad \text{(A.4)}$$

The calculated boundary compositions for AB_2 compounds with three different initial bulk compositions *i* and mass fractions of the B phase, *r*, but a fixed composition for the B phase of $B_{2.9}A_{0.1}$ (s = 0.9), are listed in Table A.1.

Table A.1 Boundary compositions for the AB_2 phase with different initial bulk composition and mass fractions of the B phase, but a fixed B phase composition.

B phase (*s*)	$A_{0.1}B_{2.9}$	$A_{0.1}B_{2.9}$	$A_{0.1}B_{2.9}$
Initial bulk composition (*i*)	$A_{0.7}B_{2.3}$	$A_{0.5}B_{2.5}$	$A_{0.3}B_{2.7}$
Mass fraction of the B phase (*r*)	0.1	0.45	0.65
AB_2 phase (*m*)	$A_{0.77}B_{2.23}$	$A_{0.83}B_{2.17}$	$A_{0.67}B_{2.33}$

If the compositions of the AB_2 phase and the B phase are both fixed, once the initial bulk composition is given, the mass fraction of the AB_2 phase or the B phase can be obtained because the initial composition and mass fraction of the B phase are interrelated. This example is similar to the case in Chapter 3, in which the boundary compositions of the solid-solution region in CTGS were obtained from the different bulk compositions (Series I, II, and III) combined with the volume fractions of the secondary phases.

The mass fraction, *r*, can be obtained for given compositions of the AB_2 phase (*m*), the B phase (*s*), and the initial bulk composition (*i*):

$$r = \frac{m - i}{m - s}. \tag{A.5}$$

The mass fraction ratio were calculated and are listed in Table A.2 for the AB_2 phases of $A_{0.77}B_{2.23}$ and the B phases of $A_{0.1}B_{2.9}$ with three different initial bulk compositions.

Table A.2 Mass fractions of the B phase for different initial bulk compositions and fixed compositions for the AB_2 and B phases.

B phase (*s*)	$A_{0.1}B_{2.9}$	$A_{0.1}B_{2.9}$	$A_{0.1}B_{2.9}$
AB_2 phase (*m*)	$A_{0.77}B_{2.23}$	$A_{0.77}B_{2.23}$	$A_{0.77}B_{2.23}$
Initial bulk composition (*i*)	$A_{0.7}B_{2.3}$	$A_{0.5}B_{2.5}$	$A_{0.3}B_{2.7}$
Mass fraction of B phase (*r*)	0.10	0.40	0.70

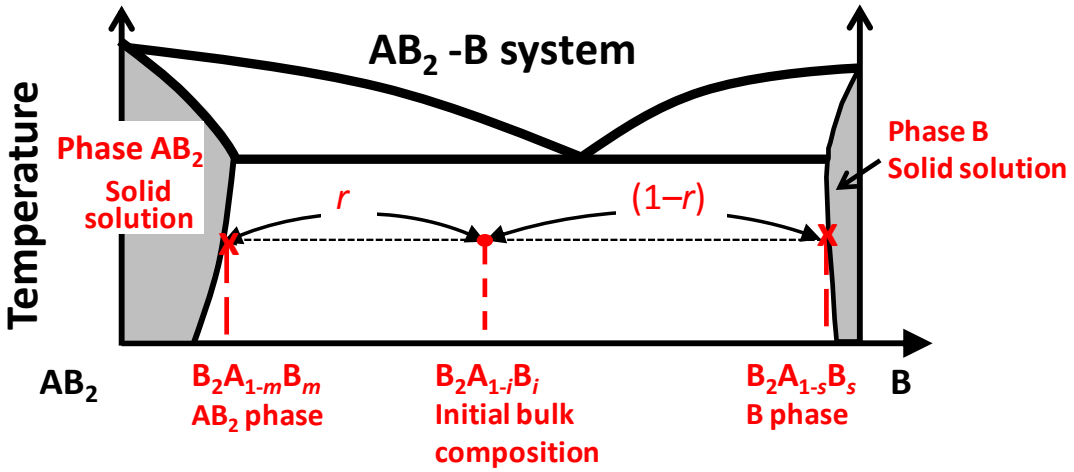

Fig. A.2 Schematic phase diagram for an AB_2–B binary system. The lever rule is applied to determine the boundary composition of the AB_2 phase using the initial bulk composition, the composition of the B phase, and the mass fraction of the B phase.

References

[1] H. Seh, H. L. Tuller, H. Fritze, *Sens. Actuators B*, **93**, 169 (2003).

[2] M. Schulz, J. Sauerwald, D. Richter, H. Fritze, *Ionics*, **15**, 157 (2009).

[3] L. Solie, J. Bracewell, *Proc. IEEE Ultrason. Symp.*, 305 (2001).

[4] A. Bungo, C. Jian, K. Yamaguchi, Y. Sawada, S. Uda, Y. P. Pisarevsky, *Jpn. J. Appl. Phys.*, **38**, 3239 (1999).

[5] A. A. Kaminskii, G. R. Verdun, B. V. Mill, A. V. Butashin, *Inorg. Mater.* **28**, 114 (1991)

[6] M. H. Randles, J. E. Creamer, R. F. Belt, G. J. Quarles, L. Esterowitz, *OSA Proceedings* (1992).

[7] H. J. Eichler, D. Ashkenasi, H. Jian, A. A. Kaminskii, *Phys. Stat. Sol.*, **146**, 833 (1994)

[8] A. E. Nosenko, V. N. Shevchu, *Phys. Solid State*, **39**, 775 (1997).

[9] E. L. Belokoneva, M. A. Simonov, A. V. Butashin, B. V. Mill, N. V. *Belov, Sov. Phys. Dokl.*, **25**, 954 (1980).

[10] B. V. Mill, A. V. Buntashin, G. G. Khodzhabagyan, E. L. Belokoneba, N. V. Belov, Dokl. Akad. *Nauk USSR*, **264**, 1385 (1982).

[11] B. V. Mill, Y. V. Pisarevsky, *Proc. 2000 IEEE/EIA Inter. Freq. Control Sympo.* 133 (2000).

[12] H. Ohsato, T. Iwataki, H. Morikoshi, *Transactions on electrical and electronic materials*, **13**(2), 51 (2012).

[13] S. Uda, S. Wang, H. Kimura, X. Huang, Ch 15, *"Crystal Growth Technology: From Fundamentals and Simulation to Large-scale Production"*, H. J. Scheel and P. Capper, Eds., Wiley-VCH, Weinheim (2008).

[14] S. Zhang, F. Yu, *J. Am. Ceram. Soc.*, **94**, 1 (2011).

[15] K. Tsukada, M. Takeuchi, S. Tokumitsu, Y. Ohmura, K. Kawaguchi, *R&D Review of Toyota CRDL*, **28** (4), 49 (1993).

[16] S. Zhang, X. Jiang, M. Lapsley, P. Moses, T. R. Shrout, *Appl. Phys. Lett.*, **96**, 013506 (2010).

[17] S. J. Zhang, Y. Q. Zheng, H. K. Kong, J. Xin, E. Frantz, T.R. Shrout, J. Appl. Phys., 105, 114107 (2009).

[18] H. Takeda, S. Tanaka, H. Shimizu, T. Nishida, T. Shiosaki, *Key Eng. Mater.*, **320**, 239 (2006).

[19] D. Damjanovic, *Curr. Opinion. Solid State Mater. Sci.* **3**, 469 (1998).

[20] H. Fritze, *J. Electroceram*, **26**, 122 (2011).

[21] T. R. Shrout, R. Eitel, C. Randall, "*High Performance, High Temperature Perovskite Piezoelectric Ceramics*", Piezoelectric Materials in Devices, Edited by N. Setter. Lausanne, Switzerland, 413, 2002.

[22] R. C. Turner, P. A. Fuierer, R. E. Newnham, T. R. Shrout, *Appl.Acoustics,* **41**, 299 (1994).

[23] S. J. Zhang, J. Luo, D. W. Snyder, T. R. Shrout, "*High Performance, High Temperature Piezoelectric Crystals*"; Handbook of Advanced Dielectric, Piezoelectric and Ferroelectric Materials – Synthesis, Characterization and Applications, Edited by Z. G. Ye. Woodhead Publishing Ltd., Cambridge, 130, 2008.

[24] S. J. Zhang, Y. T. Fei, B. H. T. Chai, E. Frantz, D. W. Snyder, X. N. Jiang, T. R. Shrout, *Appl. Phys. Lett.*, **92**, 202905 (2008).

[25] R. Yaokawa, S. Uda, H. Kimura, K. Aota, *J. Appl. Phys.*, **108**, 064112 (2010).

[26] Z. Wang, D. Yuan, X. Cheng, D. Xu, M. Lv, L. Pan, X. Duan, H. Sun, X. Shi, Y. Lv, X. Wei, Z. Sun, C. Luan, S. Guo, G. Zhang, X. Wang, *J. Crystal Growth*, **253**, 378 (2003).

[27] X. Shi, D. Yuan, X. Yin, A. Wei, S. Guo, F. Yu, *Solid State Communications*, **142**, 173 (2007).

[28] S. Kurosawa, M. Kitahara, Y. Yokota, K. Hishinuma, T. Kudo, O. Buzanov, A. Medvedev, V. Chani, A. Yoshikawa, *IEEE Transactions on Nuclear Science*, **61**, 339 (2014).

[29] D. Roshchupikin, L. Ortega, O. Plotitcyna, A. Erko, I. Zizak, D. Irzhak, R. Fahrtdinov, O. Buzanov, *Appl Phys A*, **114**, 1105 (2014).

[30] Y. Yokota, M. Sato, V. Chani, Y. Futami, K. Tota, S. Kurosawa, K. Onodera, A. Yoshikawa, *Sensors and Actuators A,* **200**, 56 (2013).

[31] L. O. Svaasand, M. Eriksrud, G. Nakken, A. P. Grande, *J. Crystal Growth*, **22**, 230 (1974).

[32] R. E. Smallmann, R. J. Bishop, "*Chapter 3: Structural Phases: Their Formation and Transitions*", Modern physical metallurgy and materials engineering. 6thed. Oxford: Butterworth-Heinemann Pub, 73 (1999).

[33] Satoshi Uda, "*Chapter 4: Stoichiometry of Oxide Crystals*", *Handbook of Crystal Growth*, Vol. IA, Fundamentals: Thermodynamics and Kinetics, and Transport and Stability, edited by T. Nishinaga,. Elsevier B.V., 175-214 (2014)

[34] H. Kimura, S. Uda, X. Huang, *J.Cryst. Growth*, **295**, 36 (2006).

[35] S. Wang, J. Harada, S. Uda, *J.Cryst. Growth*, **219**, 263 (2000).

[36] R. D. Shannon, *Acta Crystallogr*. **A32**, 751 (1976).

[37] G. Bernard-Granger, C. Guizard, *Acta Materia*, **56**, 6273 (2008).

[38] Y. Zhu, S. Wu, X. Wang, *Chem. Eng. Jour.* **175**, 512 (2011).

[39] H. Zhao, S. Uda, K. Maeda, J. Nozawa, H. Koizumi, K. Fujiwara, *J.Cryst. Growth*, **415**, 111 (2015). http://www.sciencedirect.com/science/article/pii/S002202481500007X DOI:10.1016/j.jcrysgro.2014.12.042

[40] S. Uda, H. Inaba, J. Harada, K. Hoshikawa, *J.Cryst. Growth*, **271**, 229 (2004).

[41] G. Lester, A. Clark, T. Kyser, H. Naslund, *Contrib Mineral Petrol* **166**, 329 (2013).

[42] I. Freestone, D. Hamilton, *Contrib Mineral Petrol*, **73**, 105 (1980).

[43] W. Haller, *J. Chem. Phys.* **42**,686 (1965).

[44] S. Wang, S. Uda, *J.Cryst. Growth*, **250**,463 (2003).

Publication list

1. Journal publications

Hengyu Zhao, Satoshi Uda, Kensaku Maeda, Jun Nozawa, Haruhiko Koizumi, Kozo Fujiwara, "The solid-solution region for the langasite-type $Ca_3TaGa_3Si_2O_{14}$ crystal as determined by a lever rule", *J.Cryst. Growth*, **415**, 111 (2015). (Chapter 3)

2. Oral presentations

2.1 Oral presentations (International conference)

Hengyu Zhao, Satoshi Uda, Kensaku Maeda, Jun Nozawa, Haruhiko Koizumi, Kozo Fujiwara, "Study on site occupancy of metal vacancy in langasite-type crystal with four elements", 17th International Conference on Crystal Growth and Epitaxy (ICCGE-17), Warsaw (Poland), 16. Aug. 2013.

2.2 Oral presentations (Domestic conference)

Hengyu Zhao, Jun Nozawa, Haruhiko Koizumi, Kozo Fujiwara, Satoshi Uda, "Congruency and Liquid Immiscibility in Langasite-type Crystal with Four Elements", The 62th JSAP Spring Meeting, Kanagawa, Mar. 2015.

Hengyu Zhao, Jun Nozawa, Haruhiko Koizumi, Kozo Fujiwara, Satoshi Uda, "Congruency and Liquid Immiscibility in Langasite-type Crystal with Four Elements", National Conference of Crystal Growth (NCCG-44), Tokyo, Nov. 2014.

Hengyu Zhao, Jun Nozawa, Haruhiko Koizumi, Kozo Fujiwara, Satoshi Uda, "Study on Site Occupancy of Metal-Vacancy in Langasite-type Crystals with Four Elements", The 61th JSAP Spring Meeting , Kanagawa, Mar. 2014.

Hengyu Zhao, Jun Nozawa, Kensaku Maeda, Haruhiko Koizumi, Kozo Fujiwara, Satoshi Uda, "Study on Site Occupancy of Metal-Vacancy in Langasite-type Crystals "Study on Site Occupancy of Metal-Vacancy in Langasite-type Crystals with Four

Elements", National Conference of Crystal Growth (NCCG-43), Nagano, Nov. 2013.

Hengyu Zhao, Jun Nozawa, Kensaku Maeda, Haruhiko Koizumi, Kozo Fujiwara, Satoshi Uda, "Constituent Elements and Defects Associated with Site Occupancy Freedom in Langasite-type Crystals with Four Elements", The 60th JSAP Spring Meeting, Kanagawa, Mar. 2013.

Hengyu Zhao, Jun Nozawa, Kensaku Maeda, Haruhiko Koizumi, Kozo Fujiwara, Satoshi Uda, "Investigation on Solid Solution Range of Langasite-type Crystals with Four Elements", National Conference of Crystal Growth (NCCG-42), Fukuoka, Nov. 2012.

3. Poster presentations

3.1 Poster presentations (International conference)

Hengyu Zhao, Jun Nozawa, Haruhiko Koizumi, Kozo Fujiwara, Satoshi Uda, "A study on crystal-site structure and solid solution range of langasite-type oxide crystal with four elements", 2013 Annual Meeting of Excellent Graduate Schools for "Materials Integration Center" and "Materials Science Center" in conjunction with International Workshop on Advanced Materials Synthesis Process and Nanostructure, Sendai, Mar.2014.

Hengyu Zhao, Jun Nozawa, Kensaku Maeda, Haruhiko Koizumi, Kozo Fujiwara, Satoshi Uda, "Determination of solid solution range in Langasite-type crystal with four elements", The 3rd Russia - Japan workshop "Problems of advanced materials", Novosibirsk (Russia), Oct. 2013.

Hengyu Zhao, Jun Nozawa, Kensaku Maeda, Haruhiko Koizumi, Kozo Fujiwara, Satoshi Uda, "Constituent Elements and Defects Associated with Site Occupancy Freedom in Langasite-type Crystals with Four Elements", Excellent Graduate Schools 2012 Annual Meeting in conjunction with Japan-Russia Workshop on Advanced Materials Synthesis Process and Nanostructure, Sendai, March 2013.

Hengyu Zhao, Jun Nozawa, Kensaku Maeda, Haruhiko Koizumi, Kozo Fujiwara, Satoshi Uda, "Investigation on solid solution range of langasite-type crystals with four elements", Summit of Materials Science: SMS 2012, Sendai, Nov. 2012.

Hengyu Zhao, Jun Nozawa, Kensaku Maeda, Haruhiko Koizumi, Kozo Fujiwara, Satoshi Uda, “Application of crystal lattice parameter’s measuring to determine solid solution range”, 9th Materials Science School for Young Scientists and Students 2012 (KINKEN-WAKATE2012), Sendai, Nov. 2012.

Hengyu Zhao, Jun Nozawa, Kensaku Maeda, Haruhiko Koizumi, Kozo Fujiwara, Satoshi Uda, “Melting and solidification of CNGS and CTGS sintered material measured by DTA”, International Symposium of Materials Integration In conjunction with The 2nd International Symposium on Advanced Synthesis and Processing Technology for Materials (ASPT2011), Sendai, Dec. 2011.

3.2 Poster presentations (Domestic conference)

Hengyu Zhao, Jun Nozawa, Haruhiko Koizumi, Kozo Fujiwara, Satoshi Uda, “Solid Solution Range and Liquid Immiscibility in Langasite-type Crystal with Four Elements”, 第 128 回東北大学金属材料研究所講演会, Sendai, Nov. 2014.

Hengyu Zhao, Jun Nozawa, Haruhiko Koizumi, Kozo Fujiwara, Satoshi Uda, “Congruency and Liquid Immiscibility in Langasite-type Crystal with Four Elements”, 第 127 回東北大学金属材料研究所講演会, Sendai, May. 2014.

Hengyu Zhao, Jun Nozawa, Kensaku Maeda, Haruhiko Koizumi, Kozo Fujiwara, Satoshi Uda, “Study on Site Occupancy of Metal Vacancy in Langasite-type Crystal with Four Elements”, 第 126 回東北大学金属材料研究所講演会, Sendai, Nov. 2013.

Hengyu Zhao, Jun Nozawa, Kensaku Maeda, Haruhiko Koizumi, Kozo Fujiwara, Satoshi Uda, “Constituent Elements and Defects Associated with Site Occupancy Freedom in Langasite-type Crystals with Four Elements”, 第 125 回東北大学金属材料研究所講演会, Sendai, May 2013.

Acknowledgements

The author wishes to express his sincere gratitude to Prof. Satoshi Uda of the Institute for Materials Research (IMR), Tohoku University, for his valuable help, guidance, and suggestions regarding the composition of this thesis. With instructive advice and full support of my Sensei, I can eventually achieve my goals. It is my pleasure and honor to be a part of Prof. Uda's research group, where I have witnessed excellent scientists making true contributions in material science. The spirit of rigorous scholarship and attitude towards crystal chemistry science is the most valuable lessons I learned from my Sensei.

Thanks are also due to Prof. Nagao Kobayashi and Prof. Hiromi Tobita of the Department of Chemistry, Tohoku University, for their critical reading of and constructive comments on this thesis.

In addition, I would like to express my thanks to associate Prof. Kozo Fujiwara of IMR for his instruction on the in situ observation of the crystal melting process and for his comments on my manuscript and thesis.

It is also a pleasure to acknowledge my gratitude to assistant Prof. Jun. Nozawa of IMR. Dr. Nozawa provided support for many aspects of this study, including the discussion of experiments, preparation of manuscripts for conferences, revision of journal papers, completion of applications, and composition of this thesis, all of which took much of his precious time.

Gratitude is also due to assistant Prof. Haruhiko Koizumi of IMR, researcher Dr. Wugen Pan, Dr. Xinbo Yang (presently at the Australian National University), and assistant Prof. Kensaku Maeda of the Department of Material Science and Engineering, Tohoku Univerisity, for sharing their wisdom and suggestions. Dr. Kensaku Maeda taught me the μ-PD method for growing crystals, optical observations, polishing, and interesting Japanese culture. Dr. Xinbo Yang shared his mature thinking on life and helped me to adjust to the life of a research student. The Secretary of Prof. Uda's research group, Miss Chiharu Nagura, also deserves my thanks for her kindness. She provided sweet snacks and assistance for everything necessary to me during staying in Sendai.

Deep appreciation is also extended to Prof. Kiyoshi Shimamura of the National Institute for Materials Science and Dr. Ritsuko Yaokawa of Toyota Central R&D Labs for the enlightening discussions. I am gratitude to Prof. Zengmei Wang of the College of Materials Science and Engineering, Southeast University (China), Prof. Inga G. Vasilyeva and Dr. Ruslan E. Nikolaev of the Nikolaev Institute of Inorganic Chemistry, Russian Academy of Sciences, for their suggestions in experiment designing. I am also thankful to Mr. Y. Murakami, IMR, Tohoku University, for the EPMA measurements, BEI observations, and XRD analyses, and to Mr. T. Sugawara, IMR, Tohoku University, for performing the isostatic pressing.

I also wish to thank the members of Prof. Uda's research group for their intelligence and wit: Dr. Chihiro Koyama, Miss Sumeng Hu, Miss Morgane Mokhtari, Mr. Hirotake Ide, Mr. Tomonori Tsuchiyama, Mr. Seyoun Choi, Mr. Akira Sato, Mr. Tenshin Numata, and Mr. Takashi Funada. I have wonderful memories of working with them. Thanks also go to graduated students of Prof. Uda's research group, including Dr. Raira Gotoh, Mr. Shunsuke Fujii, Mr. Yuhei Naradate, Mr. Masaya Ishii, and Mr. Kohei Suzuki, for all the interesting and fresh experiences we had together.

I wish to sincerely thank my dear parents for their understanding, sacrifices, and kind expectations. It is a great relief to know that they always support me. Last but not least, I thank my friends in Sendai, Japan, and in China. I hope that everyone I know can finally accomplish their goals and lead a happy life.

Feb. 2015